

Uncertainty in Elastic Turbulence

J. R. C. King^{1†}, R. J. Poole², C. P. Fonte³, and S. J. Lind⁴

¹Department of Mechanical and Aerospace Engineering, The University of Manchester, Manchester, UK

²Department of Mechanical and Aerospace Engineering, University of Liverpool, Liverpool, UK

³Department of Chemical Engineering, The University of Manchester, Manchester, UK

⁴School of Engineering, Cardiff University, Cardiff, UK

(Received xx; revised xx; accepted xx)

Elastic turbulence can lead to increased flow resistance, mixing and heat transfer. Its control – either suppression or promotion – has significant potential, and there is a concerted ongoing effort by the community to improve our understanding. Here we explore the dynamics of uncertainty in elastic turbulence, inspired by an approach recently applied to inertial turbulence in Ge *et al.* (2023) *J. Fluid Mech.* 977:A17. We derive equations for the evolution of uncertainty measures, yielding insight on uncertainty growth mechanisms. Through numerical experiments, we identify four regimes of uncertainty evolution, characterised by I) rapid transfer to large scales, with large scale growth rates of τ^{-6} (where τ represents time), II) a dissipative reduction of uncertainty, III) exponential growth at all scales, and IV) saturation. These regimes are governed by the interplay between advective and polymeric contributions (which tend to amplify uncertainty), viscous, relaxation and dissipation effects (which reduce uncertainty), and inertial contributions. In elastic turbulence, reducing Reynolds number increases uncertainty at short times, but does not significantly influence the growth of uncertainty at later times. At late times, the growth of uncertainty increases with Weissenberg number, with decreasing polymeric diffusivity, and with the logarithm of the maximum length scale, as large flow features adjust the balance of advective and relaxation effects. These findings provide insight into the dynamics of elastic turbulence, offering a new approach for the analysis of viscoelastic flow instabilities.

1. Introduction

Elastic turbulence Groisman & Steinberg (2000), a chaotic flow state observed in polymer solutions even in the limit of vanishing inertia, has implications across a range of application areas. It has been shown that elastic turbulence can enable emulsification (Poole *et al.* 2012); that it can promote heat transfer (Traore *et al.* 2015); that it is involved in melt fracture (Morozov & van Saarloos 2007); and that in mass-transfer limited regimes it can increase apparent reaction rates in porous reactors (Browne & Datta 2024) to provide just a few examples. Since the first documentation of elastic turbulence in 2000 by Groisman & Steinberg (2000), there has been a concerted effort amongst the community to understand the phenomenon, and we refer the reader to Steinberg (2021) and Datta *et al.* (2022) for recent and comprehensive reviews. We note the related phenomena of elasto-inertial turbulence, first described by Samanta *et al.* (2013); a chaotic state seen across a large range of Reynolds numbers, driven by the polymer dynamics, where both elastic and inertial effects are important. In this work we only

† Email address for correspondence: jack.king@manchester.ac.uk

consider two-dimensional low Reynolds number flows in the elastic turbulence regime, although the theory we develop is applicable to viscoelastic flows in general. For a review of elasto-inertial turbulence, we refer the reader to Dubief *et al.* (2023).

The work we present here was inspired by the recent work of Ge *et al.* (2023) on uncertainty in inertial (Newtonian) turbulence. In Ge *et al.* (2023), a remarkable depth of insight was provided through a relatively simple and intuitive approach: take two realisations of the Navier-Stokes equations, subtract them, and get evolution equations for the difference. The uncertainty was defined as the spatial average of the kinetic energy of the velocity difference Δu_i :

$$\langle E_\Delta \rangle = \frac{1}{V} \int \frac{1}{2} \Delta u_i \Delta u_i dV, \quad (1.1)$$

for which an evolution equation was derived. Simply by inspecting the form of the evolution equation for $\langle E_\Delta \rangle$, and performing numerical experiments in which one realisation is perturbed and the evolution of the difference is tracked, they obtained fundamental quantitative insight into the chaotic nature of turbulence: identifying a similarity regime in which the production and dissipation rates of uncertainty grow together and the uncertainty spectrum is self-similar, and that in the absence of an external input of uncertainty, uncertainty can only be created via compression events in the Newtonian case. For chaotic flows, $\langle E_\Delta \rangle$ is expected to grow exponentially, according to

$$\frac{d\langle E_\Delta \rangle}{dt} = \lambda \langle E_\Delta \rangle, \quad (1.2)$$

in which λ is twice the maximal Lyapunov exponent of the system. We are interested in chaotic flows of polymer solutions. Here, the system cannot be completely defined by the velocity field; a conformation tensor c_{ij} , which provides a macroscopic measure of the molecular deformation of polymers, is also required, and the picture is more complex.

In recent years there has been a concerted effort by the community to understand and explore the fundamental dynamics of elastic (and elasto-inertial) turbulence. Much effort has focused on the onset of instabilities, aiming to address the questions of when, where and how do viscoelastic flows transition to these chaotic states. This has led to many important discoveries, including the existence of purely elastic instabilities in straight channels (Pan *et al.* 2013), the first exact travelling wave solutions (Boffetta *et al.* 2005; Page *et al.* 2020; Morozov 2022), identification of a continuous pathway between elastic and elasto-inertial turbulence (Khalid *et al.* 2021), and the recently discovered polymer diffusive instability (Beneitez *et al.* (2023); Lewy & Kerswell (2024b,a); Couchman *et al.* (2024)) present in wall-bounded viscoelastic flows.

Early numerical studies of elastic turbulence took two-dimensional Kolmogorov flow (a flow with a uni-directional sinusoidal forcing in a doubly-periodic domain) as the setting (Berti *et al.* 2008; Berti & Boffetta 2010), and this setting is still used in more recent studies (e.g. Garg *et al.* (2021)). Even in this simple configuration, the main features observed experimentally are present: a transition to a chaotic unsteady flow state above a critical Weissenberg number; a distinct increase in power input required to sustain the flow; and an energy spectra with a power law decay having a slope steeper than k^{-3} . More recently, a similar numerical setting – doubly periodic with a cellular forcing – has been used by Plan *et al.* (2017) to estimate the Lyapunov dimension of elastic turbulence, and Gupta & Vincenzi (2019) to study the influence of polymeric diffusivity on the dynamics of elastic turbulence.

Uncertainty is inherent in both real flows of polymer solutions, and numerical simulations. The conformation tensor c_{ij} used to describe the macroscopic behaviour of

polymers is a statistical average of microscopic polymer deformations. Although if left to rest polymers will revert to an undeformed configuration ($c_{ij} \rightarrow \delta_{ij}$), in real flows of polymers, local temperature, concentration and composition fluctuations will influence viscosities and relaxation times, and potentially create local internal stresses. Consequently there is likely to be inherent uncertainty in the precise initial conditions in any real experiment. Can we ever be certain of the *exact* internal molecular configuration of polymers at the start of an experiment? In inertial (Newtonian) turbulence, thermal fluctuations have recently been shown to influence the energy cascade at the Kolmogorov length-scale in incompressible settings (Bell *et al.* 2022), and in compressible settings, this influence extends to larger length-scales, whilst intermittency is inhibited by thermal fluctuations across the entire dissipation range (Srivastava *et al.* 2025). Such findings may have implications for under-resolution approaches such as Large Eddy Simulations (LES), where closure models are used to represent the dynamics at the smallest scales. Whether such effects are significant in elastic turbulence is unknown.

For numerical simulations, a very high resolution is required to fully resolve elastic turbulence: the pseudo-spectral simulations of Berti *et al.* (2008); Berti & Boffetta (2010) were conducted with 512^2 modes, the simulations by Plan *et al.* (2017); Gupta & Vincenzi (2019) used a high-order compact finite difference scheme on a grid with 1024^2 elements, and recent studies by Lellep *et al.* (2024) use a pseudo-spectral code with $256 \times 256 \times 1024$ modes (the higher-resolution in the wall normal direction), to explore the stability of highly elastic planar channel flows. Recently, Yerasi *et al.* (2024) investigated the effect of different numerical schemes, and of polymeric diffusivity, on the large scale dynamics of numerical simulations, finding that even stable numerical simulations displaying the expected chaotic fluctuations can contain numerical errors which distort the large scale flow dynamics.

With such uncertainty inherent in viscoelastic flows, one might logically ask: how does uncertainty evolve in such settings? How will a slight under-resolution in a simulation impact the observed flow dynamics? How sensitive is an experiment to the initial conditions, or uncertainty in conditions such as flow rate, temperature, or geometry? How do effects such as thermal fluctuations or concentration fluctuations influence predictability and repeatability? These questions are also important in the development of closure models (analogous to those used for inertial turbulence): if we devise some statistical closure for the small scales, allowing the elastic turbulence equivalent of Large Eddy Simulation, how does uncertainty inherent in the small scales propagate to larger scales, and how is the long time evolution of a flow affected?

Whilst turbulence is generally analysed via spectral measures, such questions of uncertainty are more closely related with ideas around chaotic measures (Ho *et al.* 2024), such as maximum Lyapunov exponents and attractor dimension. Estimates of how the Lyapunov exponent of inertial turbulence scales date back nearly 50 years, to the work of Ruelle (1979); Deissler (1986), although a consensus on the scaling of the Lyapunov exponent with Reynolds number still eludes the community (Ge *et al.* 2023). In the field of elastic turbulence, Plan *et al.* (2017) estimated the attractor dimension based on two-dimensional numerical experiments, proposing the attractor dimension to scale with Wi^α , with $\alpha \approx 0.7$. Beyond this effort, we are not aware of any work analysing elastic turbulence via such measures.

Here we apply the concepts developed in Ge *et al.* (2023) to viscoelastic flows. In § 2 we derive evolution equations for the difference between two realisations, and from these we obtain equations governing the evolution of uncertainty in the flow and the polymer deformation. These equations provide insight into the mechanisms of uncertainty generation in viscoelastic flows in general. Focusing on the elastic turbulence regime, in

§ 3 we present a set of numerical experiments, from which we identify different regimes of uncertainty evolution, and explore how these are influenced by inertial, elastic, and length scale effects. In § 4 we draw conclusions and provide a discussion on future directions.

2. Theoretical analysis

We consider the incompressible isothermal flow of a polymer solution in a periodic domain. In dimensionless form, conservation equations for mass and momentum are

$$\frac{\partial u_i^{(m)}}{\partial x_i} = 0 \quad (2.1)$$

$$\frac{\partial u_i^{(m)}}{\partial t} + u_j^{(m)} \frac{\partial u_i^{(m)}}{\partial x_j} = -\frac{\partial p^{(m)}}{\partial x_i} + \frac{\beta}{Re} \frac{\partial^2 u_i^{(m)}}{\partial x_j \partial x_j} + \frac{(1-\beta)}{ReWi} \frac{\partial c_{ji}^{(m)}}{\partial x_j} + f_i^{(m)}, \quad (2.2)$$

where the superscript in parentheses (m) indicates the m^{th} realisation of the system, u_i is the velocity, with subscripts representing the Einstein index convention, p is the pressure, and f_i a body force. The conformation tensor c_{ji} is a macroscopic measure of the polymeric deformation. The dimensionless parameters controlling the flow are the Reynolds number Re , the Weissenberg number Wi , and the solvent to total viscosity ratio β . The polymers are assumed to obey a simplified linear PTT constitutive law (Thien & Tanner 1977), with the conformation tensor following an evolution equation given

$$\frac{\partial c_{ij}^{(m)}}{\partial t} + u_k^{(m)} \frac{\partial c_{ij}^{(m)}}{\partial x_k} - \frac{\partial u_i^{(m)}}{\partial x_k} c_{kj}^{(m)} - \frac{\partial u_j^{(m)}}{\partial x_k} c_{ik}^{(m)} = -\frac{c_{ij}^{(m)} - \delta_{ij}}{Wi} \left(1 - d\varepsilon + \varepsilon c_{kk}^{(m)}\right) + \kappa \frac{\partial^2 c_{ij}^{(m)}}{\partial x_k \partial x_k}, \quad (2.3)$$

in which κ is a dimensionless polymeric diffusivity, and $\varepsilon \geq 0$ is the sPTT nonlinearity parameter. d is the number of spatial dimensions. In the limit $\varepsilon = 0$, the Oldroyd B constitutive equation is recovered. Note in steady homogeneous flows the PTT model used here is identical to the FENE-P model.

Following Ge *et al.* (2023) we consider two realisations of (2.1) to (2.3) ($m = 1$ and $m = 2$). For time $t < t_0$, these realisations are identical. At $t = t_0$ a small perturbation is imposed on realisation (2), after which time the realisations may diverge. We define the difference between the realisations as $\Delta u_i = u_i^{(2)} - u_i^{(1)}$, $\Delta p = p^{(2)} - p^{(1)}$, and $\Delta c_{ij} = c_{ij}^{(2)} - c_{ij}^{(1)}$. We are interested in the evolution of these difference fields.

We can obtain evolution equations for Δu_i and Δc_{ij} by subtracting realisation 1 from 2 of (2.1) to (2.3). Doing so, expressing only in terms of realisation 1 and the difference, and exploiting the symmetry of $c_{ij}^{(m)}$, we obtain

$$\frac{\partial \Delta u_i}{\partial x_i} = 0 \quad (2.4)$$

$$\begin{aligned} \frac{\partial \Delta u_i}{\partial t} + u_j^{(1)} \frac{\partial \Delta u_i}{\partial x_j} + \Delta u_j \frac{\partial \Delta u_i}{\partial x_j} + \Delta u_j \frac{\partial u_i^{(1)}}{\partial x_j} = \\ -\frac{\partial \Delta p}{\partial x_i} + \frac{\beta}{Re} \frac{\partial^2 \Delta u_i}{\partial x_j \partial x_j} + \frac{1-\beta}{ReWi} \frac{\partial \Delta c_{ji}}{\partial x_j} + \Delta f_i \end{aligned} \quad (2.5)$$

$$\begin{aligned}
& \frac{\partial \Delta c_{ij}}{\partial t} + u_k^{(1)} \frac{\partial \Delta c_{ij}}{\partial x_k} + \Delta u_k \frac{\partial \Delta c_{ij}}{\partial x_k} + \Delta u_k \frac{\partial c_{ij}^{(1)}}{\partial x_k} \\
& - \frac{\partial u_i^{(1)}}{\partial x_k} \Delta c_{kj} - \frac{\partial \Delta u_i}{\partial x_k} c_{kj}^{(1)} - \frac{\partial \Delta u_i}{\partial x_k} \Delta c_{kj} - \frac{\partial u_j^{(1)}}{\partial x_k} \Delta c_{ki} - \frac{\partial \Delta u_j}{\partial x_k} c_{ki}^{(1)} - \frac{\partial \Delta u_j}{\partial x_k} \Delta c_{ki} \\
& = - \frac{\Delta c_{ij} (1 - d\varepsilon)}{Wi} + \frac{\delta_{ij} \varepsilon \Delta c_{kk}}{Wi} - \frac{\varepsilon}{Wi} \left(c_{ij}^{(1)} \Delta c_{kk} + \Delta c_{ij} c_{kk}^{(1)} + \Delta c_{ij} \Delta c_{kk} \right) \\
& \quad + \kappa \frac{\partial^2 \Delta c_{ij}}{\partial x_k \partial x_k}. \quad (2.6)
\end{aligned}$$

In the present work we restrict consideration to flows with constant, flow-independent forcing, such that $\Delta f_i = 0$, and for brevity of exposition, all terms containing Δf_i are omitted hereafter. We note here that (2.5) and (2.6) show that a non-zero difference field in *either* velocity *or* conformation tensor may evolve into a non-zero difference in both fields. There is inherent uncertainty in the conformation tensor, being a statistical average of molecular deformations, and subject to (e.g.) thermal and concentration fluctuations.

2.1. Uncertainty in the flow

We define a positive scalar metric to quantify the *uncertainty in the flow* as the kinetic energy of the velocity difference: $E_\Delta = \frac{1}{2} \Delta u_i \Delta u_i$. An evolution equation for E_Δ can be obtained by multiplying (2.5) by Δu_i , resulting in

$$\begin{aligned}
\frac{\partial E_\Delta}{\partial t} + \frac{\partial \left(u_j^{(1)} + \Delta u_j \right) E_\Delta}{\partial x_j} + \Delta u_i \Delta u_j \frac{\partial u_i^{(1)}}{\partial x_j} = - \frac{\partial \Delta u_i \Delta p}{\partial x_i} + \\
\frac{\beta}{Re} \frac{\partial}{\partial x_j} \left[\frac{\partial E_\Delta}{\partial x_j} \right] - \frac{\beta}{Re} \frac{\partial \Delta u_i}{\partial x_j} \frac{\partial \Delta u_i}{\partial x_j} + \frac{1 - \beta}{Re Wi} \Delta u_i \frac{\partial \Delta c_{ji}}{\partial x_j}. \quad (2.7)
\end{aligned}$$

We take the average of (2.7) over the periodic domain, and denoting the spatial average $\langle \cdot \rangle$ we obtain

$$\frac{d \langle E_\Delta \rangle}{dt} = \left\langle -\Delta u_i S_{ij}^{(1)} \Delta u_j \right\rangle - \left\langle \frac{\beta}{Re} \frac{\partial \Delta u_i}{\partial x_j} \frac{\partial \Delta u_i}{\partial x_j} \right\rangle + \left\langle -\frac{1 - \beta}{Re Wi} \Delta c_{ij} \Delta S_{ij} \right\rangle, \quad (2.8)$$

where $S_{ij}^{(1)} = \frac{1}{2} \left(\frac{\partial u_i^{(1)}}{\partial x_j} + \frac{\partial u_j^{(1)}}{\partial x_i} \right)$, and we have exploited the fact that $\langle \partial(\cdot)_k / \partial x_k \rangle = 0$ on the periodic domain. Note that (2.8) is only valid on periodic domains; in more general settings, the evolution of E_Δ is given by (2.7). The first two terms on the right hand side of (2.8), which (respectively) represent inertial production of uncertainty (denoted I_Δ) and viscous dissipation of uncertainty (denoted D_Δ) match those derived by Ge *et al.* (2023) for Newtonian flows. The final term represents the polymeric production of uncertainty (denoted P_Δ). We express (2.8) in these terms as

$$\frac{d \langle E_\Delta \rangle}{dt} = \langle I_\Delta \rangle - \langle D_\Delta \rangle + \langle P_\Delta \rangle. \quad (2.9)$$

Viscous dissipation D_Δ is positive by construction; Newtonian viscosity always reduces uncertainty. Inertial production may be positive or negative, and its sign is dependent on the alignment of the uncertainty velocity field Δu_i with the reference strain rate, as discussed in detail in Ge *et al.* (2023) in the context of three-dimensional inertial turbulence. Considering for now the two-dimensional case, we denote the eigenvalues of $S_{ij}^{(1)}$ as $\Lambda_i^{(1)}$ (following the convention that $\Lambda_1 \leq \Lambda_2$), and note that due to incompressibility

the two eigenvalues are equal and opposite ($\Lambda_2^{(1)} = -\Lambda_1^{(1)} = \Lambda^{(1)} > 0$). We define the components of Δu_i projected onto the corresponding principal axes as $\Delta u'_i$, and the inertial production term can be expressed as

$$\langle I_\Delta \rangle = \left\langle \Lambda^{(1)} (\Delta u_1'^2 - \Delta u_2'^2) \right\rangle, \quad (2.10)$$

in which $\Delta u'_1$ corresponds to a velocity difference aligned with the compressive flow direction in the reference field, and $\Delta u'_2$ corresponds to a velocity difference aligned with the stretching direction. This is the two-dimensional equivalent of the expression given by Ge *et al.* (2023) for three-dimensional flows: the inertial production of uncertainty is increased by uncertainty aligned with compressive flows, and decreased by uncertainty aligned with flow stretching. A similar approach may be taken to provide insight into the polymeric production of uncertainty $\langle P_\Delta \rangle$, which depends on the alignment of the uncertainty in the conformation tensor with the uncertainty in the strain rate. We again consider the two-dimensional case, and now take the principal axes of ΔS_{ij} as a local orthonormal reference frame. Denoting the eigenvalues of ΔS_{ij} as $\pm \Lambda_\Delta$ ($\Lambda_\Delta > 0$), and the components of Δc in this basis as Δc_{ij}^* , we obtain

$$\langle P_\Delta^{2D} \rangle = \left\langle \frac{1 - \beta}{Re Wi} [(\Delta c_{11}^* - \Delta c_{22}^*) \Lambda_\Delta] \right\rangle. \quad (2.11)$$

Δc_{11}^* corresponds to a difference in the polymer deformation aligned with compression in the velocity difference field, whilst Δc_{22}^* corresponds to a difference in the polymer deformation aligned with extension in the velocity difference field. We denote by ΔN_1^* the term in parentheses, which is proportional to the difference in the first normal stress difference in a basis aligned with a compressive flow difference. The polymeric production of uncertainty depends on the difference in the first normal stress difference in a basis aligned with the principal axes of the velocity difference. Little can be said a-priori of the likely sign or magnitude of ΔN_1^* , as Δc_{ij} is not constrained to remain positive definite, and even if both realisations exhibit a positive first normal stress the difference, ΔN_1^* may be negative.

Considering the viscous dissipation of uncertainty $\langle D_\Delta \rangle$, in two dimensions we may write

$$D_\Delta = \frac{\beta}{Re} \frac{\partial \Delta u_i}{\partial x_j} \frac{\partial \Delta u_i}{\partial x_j} = \frac{\beta}{Re} \left(\Delta S_{ij} \Delta S_{ij} + \frac{1}{2} \Delta \omega^2 \right), \quad (2.12)$$

where $\Delta \omega$ is the vorticity difference. As before, we can take the principal axes of ΔS_{ij} as a local orthonormal basis, and we obtain

$$D_\Delta = \frac{\beta}{Re} \left(2\Lambda_\Delta^2 + \frac{1}{2} \Delta \omega^2 \right), \quad (2.13)$$

highlighting that viscous dissipation occurs due to both differences in stretching (Λ_Δ) and rotation ($\Delta \omega$).

As a consequence of the elliptic nature of the incompressibility constraint in (2.1) and (2.2), a perturbation to the flow which is local in space can generate a non-zero uncertainty over the entire flow field instantly. For uncertainty in the flow this non-local behaviour is via the pressure gradient term in (2.5). The pressure-gradient term in (2.7) disappears on spatial averaging (i.e. it does not appear in (2.8)). Whilst it therefore does not explicitly contribute to the evolution of $\langle E_\Delta \rangle$ as a global measure of uncertainty, it does still influence the evolution of $\langle E_\Delta \rangle$, through its influence on both Δu_i and Δc_{ii} . This is verified by numerical experiments, and discussed further in § 3.

2.2. Uncertainty in polymer deformation

Identifying a suitable scalar measure of the uncertainty in the conformation tensor is non-trivial. Two requirements for such a measure are i) that it is strictly positive, and ii) that it is independent of the conformation tensor basis. Although $c_{ij}^{(1)}$ and $c_{ij}^{(2)}$ are (symmetric) positive definite, the invariants of Δc_{ij} are not necessarily positive. Several approaches are offered by Hameduddin *et al.* (2018), including the logarithmic volume ratio, and the squared distance between $c_{ij}^{(1)}$ and $c_{ij}^{(2)}$ along a geodesic curve on a Riemannian manifold. Whilst both approaches provide a strictly positive scalar measure, the derivation of evolution equations for these measures becomes prohibitively complex. For the Oldroyd B model, the elastic energy stored in the polymers is proportional to the conformation tensor trace, and a measure which can be related to the uncertainty in the stored elastic energy is desirable. We opt to take the square of the conformation tensor trace difference as a scalar measure of uncertainty on the polymeric deformation, which satisfies both the above requirements. We define $\Gamma_\Delta = (\Delta c_{ii})^2$, multiply the trace of (2.6) by $2\Delta c_{jj}$, to obtain an evolution equation for Γ_Δ :

$$\begin{aligned} \frac{\partial \Gamma_\Delta}{\partial t} + u_k^{(1)} \frac{\partial \Gamma_\Delta}{\partial x_k} + \Delta u_k \frac{\partial \Gamma_\Delta}{\partial x_k} + 2\Delta c_{jj} \Delta u_k \frac{\partial c_{ii}^{(1)}}{\partial x_k} \\ - 4\Delta c_{jj} \Delta c_{ik} S_{ik}^{(1)} - 4\Delta c_{jj} c_{ik}^{(1)} \Delta S_{ik} - 4\Delta c_{jj} \Delta c_{ik} \Delta S_{ik} \\ = -\frac{2\Gamma_\Delta}{Wi} \left[1 + 2\varepsilon c_{ii}^{(1)} + \varepsilon \Delta c_{ii} \right] + \kappa \frac{\partial^2 \Gamma_\Delta}{\partial x_k \partial x_k} - 2\kappa \frac{\partial \Delta c_{ii}}{\partial x_k} \frac{\partial \Delta c_{jj}}{\partial x_k}. \end{aligned} \quad (2.14)$$

We take the spatial average, and again exploiting the fact that any terms expressed in flux form average to zero over a periodic domain, we obtain

$$\begin{aligned} \frac{d \langle \Gamma_\Delta \rangle}{dt} = \left\langle 2\Delta c_{ii} \Delta u_k \frac{\partial c_{jj}^{(1)}}{\partial x_k} \right\rangle + \left\langle 4\Delta c_{jj} \Delta c_{ik} S_{ik}^{(1)} \right\rangle + \left\langle 4\Delta c_{jj} c_{ik}^{(1)} \Delta S_{ik} \right\rangle + \left\langle 4\Delta c_{jj} \Delta c_{ik} \Delta S_{ik} \right\rangle \\ - \left\langle \frac{2\Gamma_\Delta}{Wi} \left[1 + 2\varepsilon c_{ii}^{(1)} + \varepsilon \Delta c_{ii} \right] \right\rangle - \left\langle 2\kappa \frac{\partial \Delta c_{ii}}{\partial x_k} \frac{\partial \Delta c_{jj}}{\partial x_k} \right\rangle. \end{aligned} \quad (2.15)$$

The first term on the right hand side relates to the production of uncertainty due to advection. The next three terms originate from the upper convected derivative, and relate to production of uncertainty due to stretching and rotation of the polymers. The penultimate term corresponds to the reduction of uncertainty due to polymer relaxation. The final term is the dissipation of uncertainty due to polymeric diffusion. For convenience, we will re-write (2.15) with the terms denoted

$$\frac{d \langle \Gamma_\Delta \rangle}{dt} = \langle A_\Delta \rangle + \langle UC1_\Delta \rangle + \langle UC2_\Delta \rangle + \langle UC3_\Delta \rangle - \langle R_\Delta \rangle - \langle PD_\Delta \rangle. \quad (2.16)$$

We first comment on the effect of polymer relaxation on uncertainty. In the limit of $\varepsilon \rightarrow 0$ (the Oldroyd B limit) R_Δ is positive by construction; in the Oldroyd B limit, polymer relaxation always reduces uncertainty in the polymer deformation. For finite ε , the non-linearity in the polymer relaxation may result in (locally) negative R_Δ , when and where the inequality $c_{ii}^{(2)} > 3c_{ii}^{(1)} + 1/\varepsilon$ is satisfied. Certainly in the early stages of uncertainty evolution, when the two fields are closely correlated, we would not expect this to occur. With the two realisations following the same evolution equations, and expected to have the same statistics, we would not expect $\langle R_\Delta \rangle < 0$ either. Indeed, $\langle R_\Delta \rangle$ remains positive throughout all our numerical simulations, and in fact we see a trend that $\langle R_\Delta \rangle / \langle \Gamma_\Delta \rangle$ increases with increasing ε . The term $\langle PD_\Delta \rangle$ is positive by

construction; polymeric diffusion always reduces uncertainty in the polymer deformation. The production of uncertainty in polymer deformation due to advection $\langle A_\Delta \rangle$, and due to stretching and rotation, $\langle UC1_\Delta \rangle$, $\langle UC2_\Delta \rangle$, and $\langle UC3_\Delta \rangle$, may be either positive or negative. Considering the term $\langle UC1_\Delta \rangle$, we take the principal axes of $S_{ij}^{(1)}$ as a local orthonormal basis, and we denote the components of Δc in this basis as $\Delta c'_{ij}$. Expressed in this basis, we can write

$$UC1_\Delta = 4\Lambda^{(1)} (\Delta c'_{22} - \Delta c'_{11}), \quad (2.17)$$

where $\Delta c'_{11}$ represents deformation in the conformation tensor difference aligned with compressive flow in the reference field, and $\Delta c'_{22}$ represents that aligned with stretching flow. From (2.17), we see that regions of extensional deformation in the conformation tensor difference aligned with extensional flow promote uncertainty, whilst extensional deformation in the conformation tensor difference aligned with compressive flow reduce uncertainty. Next considering the term $\langle UC2_\Delta \rangle$, and taking the principal axes of ΔS_{ij} as a local orthonormal basis, we write

$$UC2_\Delta = 4\Delta c_{ii}\Lambda_\Delta (c_{22}^{(1)*} - c_{11}^{(1)*}), \quad (2.18)$$

in which $c_{22}^{(1)*}$ and $c_{11}^{(1)*}$ correspond to polymeric deformation in the reference field aligned with stretching and compression (respectively) in the velocity difference field. Whether or not this term is positive or negative depends on the sign of the conformation tensor trace difference, and the normal stress difference in the reference field aligned with the principal stretching direction of the velocity difference. The term $\langle UC3_\Delta \rangle$ is constructed from the product of three differences, whilst the terms $\langle UC1_\Delta \rangle$ and $\langle UC2_\Delta \rangle$ are each formed of the product of two differences and a reference field. Hence, whilst the two realisations are largely correlated and uncertainty is small, we expect the term $\langle UC3_\Delta \rangle$ to be small relative to the other two upper convected terms. The term in (2.15) relating to the advection of polymers contains only invariants of the conformation tensor and its difference. If we take the principal axes of $c_{ij}^{(1)}$ as a local orthonormal basis, and denote tensors expressed in this basis, and vectors projected onto this basis, with a double prime, we can express the advection term in (2.15) as

$$A_\Delta = 2\Delta c_{ii}\Delta u_k'' \frac{\partial c_{jj}^{(1)}}{\partial x_k''}. \quad (2.19)$$

A characteristic of elastic turbulence is thin regions of highly deformed polymers, and here the gradient of the conformation tensor trace $\partial c_{ii}^{(1)}/\partial x_k$ will be predominantly aligned normal to the principal stretching direction of the polymers. Hence, we expect $\partial c_{jj}^{(1)}/\partial x_1'' \gg \partial c_{jj}^{(1)}/\partial x_2''$ in regions of large polymer deformation. Noting that Δc_{ii} may be negative, but whilst the two realisations are still predominantly correlated, $|\Delta c_{ii}|$ is likely to be larger in regions where $c_{ii}^{(1)}$ is large, we may expect $\langle A_\Delta \rangle$ to depend on the relative orientation of the uncertainty in the velocity, and the reference polymer deformation. Such analysis can only provide a certain amount of insight, and to investigate the dynamics of uncertainty further, we turn to numerical simulations.

3. Numerical Experiments

We conduct numerical experiments on the system described in §2. We consider two-dimensional realisations of (2.1) to (2.3) on a doubly-periodic domain with (integer) side length n , subject to a constant cellular forcing. The system is non-dimensionalised by

the forcing wavelength and the velocity magnitude of the Newtonian laminar fixed point, and setting the forcing $f_1 = f_0 \sin(2\pi x_2)$, $f_2 = f_0 \sin(2\pi x_1)$, with $f_0 = 4\pi^2/Re$ gives, for the Newtonian case ($\beta \rightarrow 1$ or $Wi \rightarrow 0$) at small Re , a stable laminar fixed point $u_1 = \sin(2\pi x_2)$, $u_2 = \sin(2\pi x_1)$. We note that this configuration is closely related to those studied in Plan *et al.* (2017), but with a different non-dimensionalisation: we take the forcing scale as the characteristic lengthscale, and impose a forcing magnitude inversely proportional to Re , whilst Plan *et al.* (2017) take the domain size as the characteristic length scale, and do not provide information on the relationship between f_0 and Re .

We numerically solve (2.1) to (2.3) using a pseudo-spectral code built within the Dedalus framework (Burns *et al.* 2020). The domain is discretised with 128 Fourier modes per forcing wavelength (i.e. the entire domain is discretised with $(128n)^2$). The system is integrated in time with a 2^{nd} order Runge-Kutta scheme, and except where explicitly stated, we use a fixed time step of $\delta t = 4 \times 10^{-4}$. We base our experiments around a reference configuration with $Re = 10^{-2}$, $\beta = 1/2$, $\varepsilon = 0$, $\kappa = 2.5 \times 10^{-5}$, $n = 4$, $Wi = 2$. We include a polymeric diffusivity term in our simulations to provide numerical stability. As explored in detail in Gupta & Vincenzi (2019), care must be taken when including polymeric diffusivity in a numerical simulation. Morozov (2022) uses a polymeric diffusivity justified by kinetic theory, and the value we use, κ , is slightly smaller than this value. We note however that whilst Morozov (2022) was exploring the onset of instabilities, we are investigating the dynamics of an established chaotic state. Consequently, our results are not independent of κ . Due to the chaotic nature of the flow, and the sensitivity to perturbations which we will explore in the following sections, this dependence on polymeric diffusivity is expected: for a chaotic flow, we expect the evolution of two realisations with the same initial conditions and differing only by a small change in the polymeric diffusivity $\Delta\kappa$ to diverge over time.

Additional simulations of the reference configuration at higher resolution ($(192n)^2$ modes) confirm resolution independence. The simulations are run for 200 time units to allow initial transients to decay. For the largest domain sizes and Weissenberg numbers considered, this is more than 10 times the maximum timescale of the flow. Statistics are then gathered for a further 200 time units. Between $(128n)^2$ and $(192n)^2$ modes the discrepancy in the mean kinetic energy is 0.35%, and the standard deviation of the kinetic energy differs by 1.6%. In the Oldroyd B limit ($\varepsilon = 0$), there are lower bounds on the conformation tensor trace ($c_{ii} \geq 2$ in two-dimensions) and its determinant ($\det c \geq 1$) (Hu & Lelièvre 2007): values below these bounds represent non-physical configurations of polymer deformation, and it has recently been shown by Yerasi *et al.* (2024) that failing to satisfy these constraints can result in a numerical simulation exhibiting significantly modified large scale flow dynamics. Although these criteria are not enforced by construction in our numerical framework, we confirm that the resolution we use is sufficient that both are met. The left panel of figure 1 shows the energy spectra of the flow for two resolutions. Note that here, and in all other spectra calculated in this work, the wavenumbers have been normalised by the forcing wavenumber (indicated by a vertical dotted red line). There is a close agreement in the energy spectra up to the Nyquist wavenumber of the more coarse resolution. The energy spectra shows a power law decay, with a slope of approximately 3.7 (indicated in figure 1 by a dashed black line), characteristic of the elastic turbulent regime. The right panel of figure 1 shows a snapshot of the vorticity field for the reference configuration.

For each configuration we run a precursor simulation for 300 time units (realisation 1). Realisation 2 is initialised by restarting the simulation from realisation 1 at a specified time $t_0 > 200$, and subject to a small perturbation. We then track the evolution of the

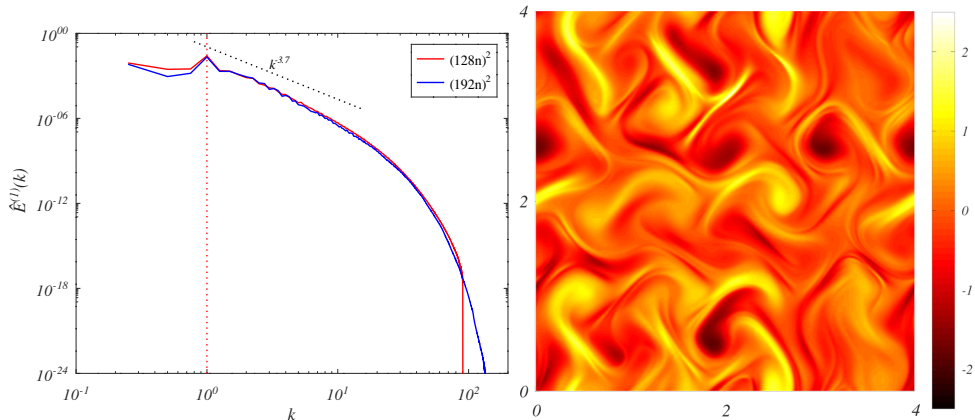


FIGURE 1. Left panel: The kinetic energy spectra of the flow in the reference configuration, for two resolutions $(128n)^2$ and $(192n)^2$. Right panel: a snapshot of the vorticity field for the reference configuration.

difference between the two realisations. We denote the time after the perturbation is imposed as $\tau = t - t_0$. The perturbation is imposed by the addition of the term

$$-A_0 \exp \left[- \left(\frac{\tau}{\delta_{t0}} \right)^2 \right] \frac{\partial^4 c_{ij}^{(2)}}{\partial x_k \partial x_k \partial x_l \partial x_l} \quad \forall \tau \geq 0 \quad (3.1)$$

to the right hand side of (2.3). The parameter δ_{t0} controls the temporal extent of the perturbation, and we use $\delta_{t0} = 10^{-3}$ throughout. A_0 controls the magnitude of the perturbation, and except where explicitly stated, we set $A_0 = 2.5 \times 10^{-8}$. This perturbation acts directly on the conformation tensor, and suppresses high wavenumber modes. We have investigated reducing δ_{t0} , such that $\delta_{t0} \ll \delta t$, where δt is the time step used in the numerical framework, and find that although the magnitude of the uncertainty is reduced (the integral of the term in (3.1) is smaller) this does not influence the evolution of uncertainty.

The temporal evolution of the spatially averaged quantities exhibits a dependence on the reference flow. Hence, for each configuration we conduct 10 simulations for $t_0 \in [200, 210, 220, 230, 240, 250, 260, 270, 280, 290]$. Simulations are run until $\tau = 50$, allowing the uncertainty to reach a statistically steady state for the reference configuration. Except where stated in the following, when plotting the time evolution of spatially averaged quantities, we show the ensemble average across these 10 simulations. For strictly positive spatially averaged quantities which evolve over many orders of magnitude (e.g. $\langle E_\Delta \rangle$ and $\langle \Gamma_\Delta \rangle$), the ensemble average is taken as the geometric mean. For normalisation purposes, we define an average total energy as

$$E_{avg}^{(tot)} = \frac{1}{\tau_0} \int_0^{\tau_0} \langle E^{(1)} \rangle + \langle E^{(2)} \rangle d\tau, \quad (3.2)$$

where $\tau_0 = 50$ time units, the duration of the simulation.

3.1. The evolution of uncertainty

The left panel of figure 2 shows the evolution of $\langle E_\Delta \rangle / E_{avg}^{(tot)}$ and $\langle \Gamma_\Delta \rangle / Wi^2$ with τ , for individual instances (red lines), and the ensemble average (blue lines). There is a clear period of exponential growth, over approximately 6 orders of magnitude, with the same exponent in both $\langle E_\Delta \rangle / E_{avg}^{(tot)}$ and $\langle \Gamma_\Delta \rangle / Wi^2$. This exponential growth starts at $\tau \approx 1$

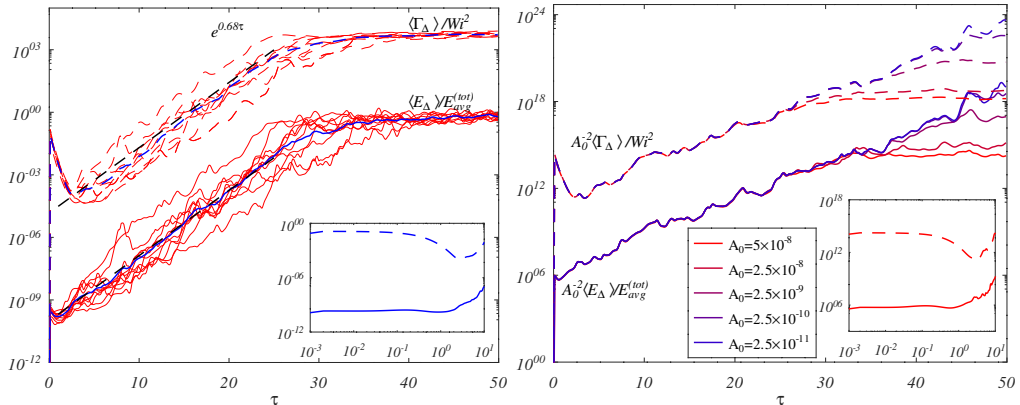


FIGURE 2. Left panel: the evolution of $\langle E_\Delta \rangle / E_{avg}^{(tot)}$ and $\langle \Gamma_\Delta \rangle / Wi^2$ for the reference configuration ($Re = 10^{-2}$, $\beta = 1/2$, $\varepsilon = 0$, $\kappa = 2.5 \times 10^{-5}$, $n = 4$, $Wi = 2$). Red lines indicate the evolution for individual simulations, whilst blue lines indicate the average. Right panel: the evolution of $A_0^{-2} \langle E_\Delta \rangle / E_{avg}^{(tot)}$ and $A_0^{-2} \langle \Gamma_\Delta \rangle / Wi^2$ for a range of values of A_0 . In both panels, the inset shows the evolution of uncertainty at small τ .

for the flow uncertainty, and $\tau \approx 3$ for $\langle \Gamma_\Delta \rangle$. As observed by Berti *et al.* (2008); Berti & Boffetta (2010) for elastic turbulence driven by a Kolmogorov forcing, there is a strong imprint of the laminar fixed point in the chaotic flow field, and as a consequence there is a limit to the uncertainty (the extent to which the two realisations can decorrelate). This is clear in the left panel of figure 2 as both $\langle E_\Delta \rangle / E_{avg}^{(tot)}$ and $\langle \Gamma_\Delta \rangle / Wi^2$ reach limiting values of approximately 0.3 and 2000 (respectively) after approximately 30 time units. Note that $\left\langle \left(c_{ii}^{(1)} \right)^2 + \left(c_{ii}^{(2)} \right)^2 \right\rangle / Wi^2 \approx 6645$, and the saturation value of $\langle \Gamma_\Delta \rangle / Wi^2$ is about 0.3 times this. From these results we can identify four regimes: (I) very short time growth $\langle E_\Delta \rangle$ and $\langle \Gamma_\Delta \rangle$ until $\tau \approx 0.1$; (II) a reduction in uncertainty, initially in $\langle \Gamma_\Delta \rangle$, over timescales of the order of unity; (III) exponential growth of uncertainty, initially in $\langle E_\Delta \rangle$ from $\tau \approx 1$, then also $\langle \Gamma_\Delta \rangle$ from $\tau \approx 4$; and (IV) saturation of uncertainty from $\tau \approx 30$. We discuss the mechanisms controlling these regimes further below. Note, we have run simulations for an additional 150 time units, up to $\tau = 200$, and do not observe any further growth in uncertainty. During the exponential regime (III), the evolution of the quantities $\langle E_\Delta \rangle$ and $\langle \Gamma_\Delta \rangle$ can be modelled by

$$\frac{d\langle E_\Delta \rangle}{dt} = \lambda \langle E_\Delta \rangle; \quad \frac{d\langle \Gamma_\Delta \rangle}{dt} = \lambda \langle \Gamma_\Delta \rangle \quad (3.3)$$

in which λ is a characteristic growth rate, equal to twice the maximal Lyapunov exponent. Letting $\{\cdot\}_{(III)}$ represent the temporal mean of a quantity over regime (III), we calculate $\{\lambda\}_{(III)} = 0.68$. This growth rate is shown by the dashed black lines in the left panel of figure 2.

The right panel of figure 2 shows the evolution of $\langle E_\Delta \rangle / E_{avg}^{(tot)}$ with τ for different values of A_0 , with results scaled by A_0^{-2} , for a single simulation. Prior to the saturation of uncertainty, the lines collapse, as the magnitude of the uncertainty scales with A_0^2 , the square of the perturbation amplitude, by definition of E_Δ and Γ_Δ . Just as the evolution of uncertainty is independent of δ_{t_0} it is unchanged by the magnitude of A_0 , despite the magnitude of the perturbation changing by over three orders of magnitude. The imprint of the reference flow on the uncertainty is visible the right panel of figure 2, where for all values of A_0 the same reference flow is used.

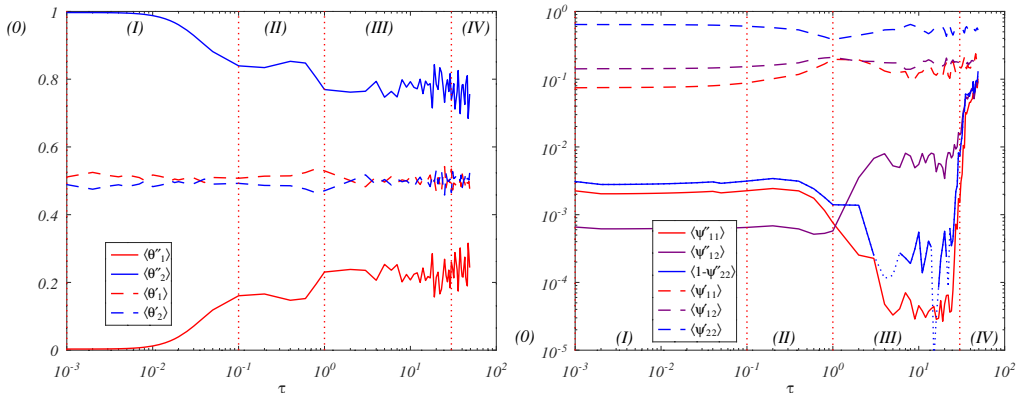


FIGURE 3. The evolution of the orientation of uncertainty for the reference configuration ($Re = 10^{-2}$, $\beta = 1/2$, $\varepsilon = 0$, $\kappa = 2.5 \times 10^{-5}$, $n = 4$, $Wi = 2$). Left panel: the evolution of $\langle \theta' \rangle$ and $\langle \theta'' \rangle$. Right panel: the evolution of components of $\langle \psi' \rangle$ and $\langle \psi'' \rangle$. Note the components of $\langle \psi'' \rangle$ may be greater than unity, and where we have plotted $\langle 1 - \psi''_{22} \rangle$ and this quantity is negative, it is plotted with a dotted line. The different regimes of uncertainty evolution are indicated separated by dotted red vertical lines.

3.1.1. The orientation of uncertainty

As before, we take the principal axes of the reference strain rate tensor $S_{ij}^{(1)}$ to define a local orthonormal basis (denoted with a prime). We also use the principal axes of the reference conformation tensor $c_{ij}^{(1)}$ to define another basis (denoted with a double prime). We use each basis to obtain a projection of the flow uncertainty Δu_i , which we denote $\Delta u'_i$ and $\Delta u''_i$. We also express the uncertainty in the conformation tensor in these bases (denoted $\Delta c'_{ij}$ and $\Delta c''_{ij}$). We denote the proportion of the uncertainty energy aligned with each principal direction as

$$\theta'_i = \frac{\Delta u_i'^2}{2 \langle E_\Delta \rangle}, \quad (3.4)$$

where an equivalent definition follows for θ''_i . Note that $\theta'_1 + \theta'_2 = \theta''_1 + \theta''_2 = 1$. The quantity θ'_1 represents the proportion of uncertainty energy aligned with compressive flow and θ'_2 represents the proportion aligned with stretching flow. The quantity θ''_2 represents the proportion of uncertainty energy aligned with the principal stretching direction of the conformation tensor, and θ''_1 is the proportion of uncertainty energy orthogonal to this.

In Ge *et al.* (2023), they observed an uneven distribution of the orientation of the uncertainty energy for three-dimensional turbulence in a Newtonian fluid: during the similarity regime characterised by exponential growth of uncertainty, the majority of the uncertainty energy was aligned with the compressive flow direction. The picture is different in the two-dimensional low Re elastic turbulence case. The left panel of figure 3 shows the evolution of $\langle \theta' \rangle$ and $\langle \theta'' \rangle$. The variation of $\langle \theta'_1 \rangle$ is small: at all times $0.467 \leq \langle \theta'_1 \rangle \leq 0.542$; the uncertainty energy is approximately evenly split between regions of compression and extension. There does not appear to be any preferential orientation of uncertainty energy due to the reference flow. The relative orientation of the velocity difference field and the reference flow field only appears in (2.8) in the inertial production term, and for small Re , this is small. At early times, the quantity $\langle \theta''_1 \rangle$ is very small, and $\langle \theta''_2 \rangle \approx 1$; i.e., the perturbation we impose in the conformation tensor is predominantly aligned with the direction of polymer extension. During regime (I) ($\tau \lesssim 0.1$), the orientation changes, and $\langle \theta''_1 \rangle$, the proportion of the uncertainty energy $\langle E_\Delta \rangle$ perpendicular to the extensional direction of the polymers, increases to

approximately 0.15. There is a further increase in $\langle \theta_1'' \rangle$ during regime (II) ($0.1 \lesssim \tau \lesssim 1$), and during regime (III) ($1 \lesssim \tau \lesssim 30$), $\langle \theta_1'' \rangle \approx 0.25$. During the exponential growth regime approximately a quarter of the uncertainty energy is aligned perpendicular to the direction of polymeric extension. The increase in the proportion of the uncertainty energy aligned normal to the principal direction of reference polymer deformation prior to regime (III) is consistent with the analysis in § 2; we expect the production of uncertainty due to polymer advection $\langle A_\Delta \rangle$ to be larger when the uncertainty energy is aligned with the gradient of the polymer deformation trace, which we expect to be normal to the primary polymer deformation. In regime (IV) ($\tau \gtrsim 30$), there is a slight further increase in $\langle \theta_1'' \rangle$. That $\langle \theta_1'' \rangle$ always remains below approximately 0.3 is further indication that there is a limit to complete decorrelation: both realisations are subject to the same forcing, and even when their evolutions are fully diverged, the imprint of the forcing in each flow results in a residual correlation.

As a measure of the relative orientation of the uncertainty in the conformation tensor we define

$$\psi'_{ij} = \frac{\Delta c_{ij}'^2}{\langle \Gamma_\Delta \rangle}, \quad (3.5)$$

with an equivalent definition for ψ''_{ij} . We note here that because (in two dimensions) $\Gamma_\Delta = (\Delta c_{ii})^2 = \Delta c_{11}^2 + \Delta c_{22}^2 + \Delta c_{11} \Delta c_{22}$, and $\Delta c_{11} \Delta c_{22}$ may be positive or negative, it is possible to have $\psi'_{ij} > 1$. The right panel of figure 3 shows the evolution of $\langle \psi' \rangle$ and $\langle \psi'' \rangle$.

At all times the largest component of $\langle \psi' \rangle$ is $\langle \psi'_{22} \rangle$, and the largest component of $\langle \psi'' \rangle$ is $\langle \psi''_{22} \rangle$ - the largest component of the elastic uncertainty energy is aligned with stretching and polymeric extension in the reference flow. During regime (II) this proportion decreases, from approximately 0.6 to approximately 0.35 at $\tau = 1$, before increasing again during regime (III) to approximately 0.5. Following the expression for $UC1_\Delta$ in (2.17), this implies that $\langle UC1_\Delta \rangle$ will be positive at all times. We next inspect the evolution of $\langle \psi'' \rangle$. Note that in the right panel of figure 3 we have plotted $\langle \psi''_{11} \rangle$, $\langle \psi''_{12} \rangle$ and $\langle 1 - \psi''_{22} \rangle$. At short times the orientation of the elastic energy of uncertainty relative to the reference polymeric deformation is roughly constant, with $\langle \psi''_{22} \rangle \approx 0.997$. At the start of regime (III), from $\tau \approx 1$ to $\tau \approx 4$, $\langle \psi''_{22} \rangle$ increases (to approximately 1). This period coincides with exponential growth starting in $\langle E_\Delta \rangle$ whilst $\langle \Gamma_\Delta \rangle$ continues to decay. As we will discuss later, during this period, uncertainty is growing exponentially at large scales, but is reducing due to polymeric dissipation and relaxation at small scales. During this period at the start of regime (III), there is also a decrease in $\langle \psi''_{11} \rangle$, and an increase in $\langle \psi''_{12} \rangle$. During the transition to exponential growth, a greater proportion of the elastic energy of uncertainty is deviatoric in an orthonormal basis aligned with the reference polymeric deformation, indicating a rotation of the elastic energy of uncertainty relative to the polymeric deformation of the reference field as the two realisations decorrelate. However, we note that for the remainder of regime (III) ($4 \lesssim \tau \lesssim 30$) the orientation of elastic energy of uncertainty is roughly constant with respect to the reference polymeric deformation. At the end of regime (III), there is a sharp decrease in $\langle \psi''_{22} \rangle$ ($\langle 1 - \psi''_{22} \rangle$ increases by two orders of magnitude), and a corresponding increase in $\langle \psi''_{11} \rangle$ and $\langle \psi''_{12} \rangle$.

3.1.2. Terms contributing to the evolution of $\langle E_\Delta \rangle$

We now consider how the terms in (2.8) evolve. The left panel of figure 4 shows the evolution of $d\langle E_\Delta \rangle/dt$, and the terms contributing to $d\langle E_\Delta \rangle/dt$ in (2.8). Note that we have calculated $d\langle E_\Delta \rangle/dt$ with a first order forward difference approximation based on successive values of $\langle E_\Delta \rangle$ separated by $\delta\tau = 10^{-3}$. There is very close agreement

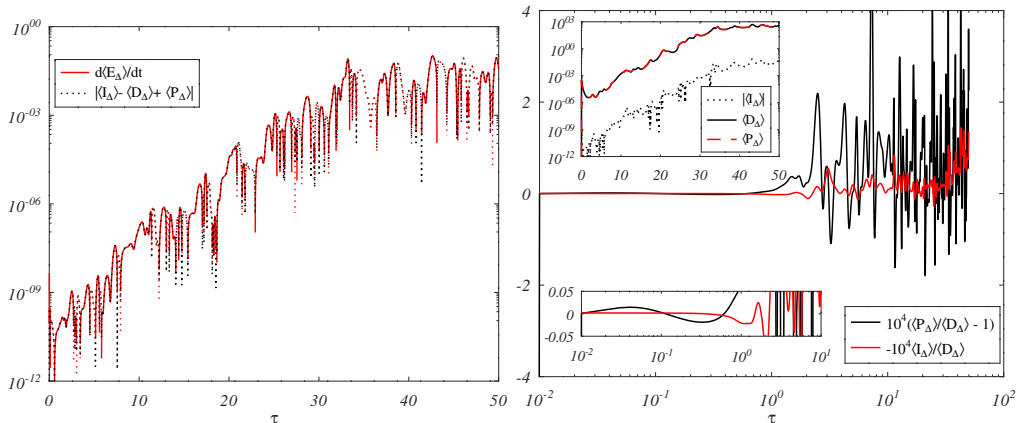


FIGURE 4. The evolution of $d\langle E_\Delta\rangle/dt$ and terms in (2.8) for the reference configuration ($Re = 10^{-2}$, $\beta = 1/2$, $\varepsilon = 0$, $\kappa = 2.5 \times 10^{-5}$, $n = 4$, $Wi = 2$). The left panel shows the sum of terms in (2.8) and the calculated values of $d\langle E_\Delta\rangle/dt$. Where $d\langle E_\Delta\rangle/dt > 0$, a solid red line is used, and where $d\langle E_\Delta\rangle/dt < 0$, a dotted red line. The right panel shows ratios of the terms in (2.8). The lower inset highlights the early-time evolution. The upper inset shows the evolution of the individual terms $\langle I_\Delta\rangle$, $\langle D_\Delta\rangle$, and $\langle P_\Delta\rangle$.

between the calculated value of $d\langle E_\Delta\rangle/dt$ and $\langle I_\Delta\rangle - \langle D_\Delta\rangle + \langle P_\Delta\rangle$, providing confirmation that (2.8) holds. The right panel of figure 4 shows the evolution of the ratios $-\langle I_\Delta\rangle/\langle D_\Delta\rangle$ and $\langle P_\Delta\rangle/\langle D_\Delta\rangle - 1$ (scaled by 10^4). The upper inset shows the individual terms $\langle I_\Delta\rangle$, $\langle P_\Delta\rangle$, and $\langle D_\Delta\rangle$. Firstly, we note that $\langle I_\Delta\rangle$ is almost always negative (we have plotted $|\langle I_\Delta\rangle|$ in the inset), indicating that in this regime the (small) net effect of the inertial terms is to reduce uncertainty. The quantities $\langle P_\Delta\rangle$ and $\langle D_\Delta\rangle$ are closely matched, and approximately 4 orders of magnitude larger than $\langle I_\Delta\rangle$. The quantity $\langle P_\Delta\rangle/\langle D_\Delta\rangle - 1$ provides a measure of this match: for $\langle P_\Delta\rangle/\langle D_\Delta\rangle - 1 > 0$, polymeric production of uncertainty outweighs viscous dissipation of uncertainty. For $\langle P_\Delta\rangle/\langle D_\Delta\rangle - 1 < 0$, viscous dissipation dominates. The evolution of $\langle P_\Delta\rangle/\langle D_\Delta\rangle - 1$ shows several distinct behaviours. At very early times (lower inset) the quantity $\langle P_\Delta\rangle/\langle D_\Delta\rangle - 1$ is positive, indicating the early stage increase in uncertainty is driven by polymeric production. Subsequently, $\langle P_\Delta\rangle/\langle D_\Delta\rangle - 1$ becomes negative on timescales of the order of 10^{-1} . In this period, there is a net reduction in uncertainty as viscous dissipation dominates polymeric production. From $\tau \approx 1$ to $\tau \approx 25$, $\langle P_\Delta\rangle/\langle D_\Delta\rangle - 1$ fluctuates, but is predominantly positive. This period corresponds to the regime of exponential growth of uncertainty. As uncertainty saturates, the quantity $\langle P_\Delta\rangle/\langle D_\Delta\rangle - 1$ increases, with a trend matching that of $-\langle I_\Delta\rangle/\langle D_\Delta\rangle$.

3.1.3. Terms contributing to the evolution of $\langle \Gamma_\Delta\rangle$

Figure 5 shows the evolution of $d\langle \Gamma_\Delta\rangle/dt$, and the contributing terms in (2.15). The left panel shows the evolution of $d\langle \Gamma_\Delta\rangle/dt$ (evaluated from successive values of $\langle \Gamma_\Delta\rangle$ at intervals of $\delta\tau = 10^{-3}$), and the sum of the terms in the right hand side of (2.15). The two quantities match very closely, with discrepancies only arising when $d\langle \Gamma_\Delta\rangle/dt$ is rapidly changing, due to the first order finite difference approximation used to evaluate $d\langle \Gamma_\Delta\rangle/dt$.

The right panel of figure 5 shows the evolution of the individual terms in (2.15). For this configuration with $\varepsilon = 0$ (i.e. Oldroyd B), theoretically $\langle R_\Delta\rangle = \langle 2\Gamma_\Delta/Wi\rangle = \langle \Gamma_\Delta\rangle$. We first consider the upper convected terms. $\langle UC1_\Delta\rangle$ is at all times positive. This observation is consistent with the finding in § 3.1.1 that $\langle \psi'_{22}\rangle$ is always the largest component of

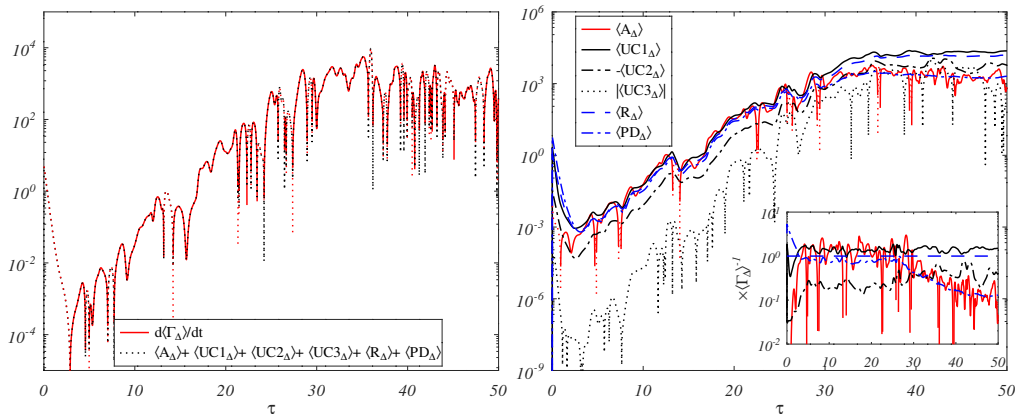


FIGURE 5. The evolution of $d\langle\Gamma_{\Delta}\rangle/dt$ and terms in (2.15) for the reference configuration ($Re = 10^{-2}$, $\beta = 1/2$, $\varepsilon = 0$, $\kappa = 2.5 \times 10^{-5}$, $n = 4$, $Wi = 2$). The left panel shows the sum of terms in (2.15) and the calculated values of $d\langle\Gamma_{\Delta}\rangle/dt$. Where $d\langle\Gamma_{\Delta}\rangle/dt > 0$, a solid red line is used, and where $d\langle\Gamma_{\Delta}\rangle/dt < 0$, a dotted red line. The right panel shows the individual terms in (2.15). The inset shows these same terms normalised by $\langle\Gamma_{\Delta}\rangle$. Where $\langle A_{\Delta}\rangle$ is negative, it is plotted with a dotted red line, and with a solid red line where positive.

$\langle\psi'\rangle$. Stretching in the conformation tensor difference field is predominantly aligned with stretching in the reference flow, and this contributes to an increase in uncertainty. $\langle UC2_{\Delta}\rangle$ is at all times negative (note we have plotted $-\langle UC2_{\Delta}\rangle$), and always approximately an order of magnitude smaller than $\langle UC1_{\Delta}\rangle$. $\langle UC3_{\Delta}\rangle$ is sometimes positive and sometimes negative, and with magnitude several orders smaller than $\langle UC1_{\Delta}\rangle$, as predicted in § 2. The relative importance of $\langle UC3_{\Delta}\rangle$ increases with time as the uncertainty increases, but even in regime (IV) it remains an order of magnitude smaller than the other two upper convected terms. Of the upper convected terms, it is $\langle UC1_{\Delta}\rangle$ which dominates the dynamics of uncertainty evolution, with $\langle UC2_{\Delta}\rangle \sim -0.1\langle UC2_{\Delta}\rangle$ through regime (III), and $\langle UC1_{\Delta}\rangle > 0$ at all times. The net contribution of the upper convected terms is to amplify uncertainty.

The inset of the right panel of figure 5 shows the evolution of the terms in (2.15) normalised by $\langle\Gamma_{\Delta}\rangle$. At early times, $\langle PD_{\Delta}\rangle$ dominates, as the perturbation is focused at small scales. Over the first few time units, the relative magnitude of $\langle PD_{\Delta}\rangle$ reduces, and during the exponential regime ($\tau \in [1, 30]$), we see $\langle PD_{\Delta}\rangle \approx \langle R_{\Delta}\rangle = \langle\Gamma_{\Delta}\rangle$. During the period of exponential growth of $\langle\Gamma_{\Delta}\rangle$, the ratio $\langle UC1_{\Delta}\rangle/\langle\Gamma_{\Delta}\rangle$ is always greater than unity, and the ratio $\langle PD_{\Delta}\rangle/\langle\Gamma_{\Delta}\rangle$ is always less than unity. The growth of uncertainty is approximately determined by the balance of the quantity

$$\frac{\langle UC1_{\Delta}\rangle + \langle A_{\Delta}\rangle - \langle R_{\Delta}\rangle - \langle PD_{\Delta}\rangle}{\langle\Gamma_{\Delta}\rangle}, \quad (3.6)$$

which is equivalent (neglecting the contributions of $\langle UC2_{\Delta}\rangle$ and $\langle UC3_{\Delta}\rangle$), to twice the maximal Lyapunov exponent of $\langle\Gamma_{\Delta}\rangle$. With $\langle R_{\Delta}\rangle = \langle\Gamma_{\Delta}\rangle$, and $\langle UC1_{\Delta}\rangle$ and $\langle PD_{\Delta}\rangle$ closely correlated to $\langle\Gamma_{\Delta}\rangle$, it is the advective term which largely determines whether uncertainty increases or reduces (note that this advective term, originating from (2.3), remains relevant even at very low Re). This can be seen in figure 5, where regions of negative $\langle A_{\Delta}\rangle$ (shown with a dotted red line), correspond to short term decreases in $\langle R_{\Delta}\rangle$.

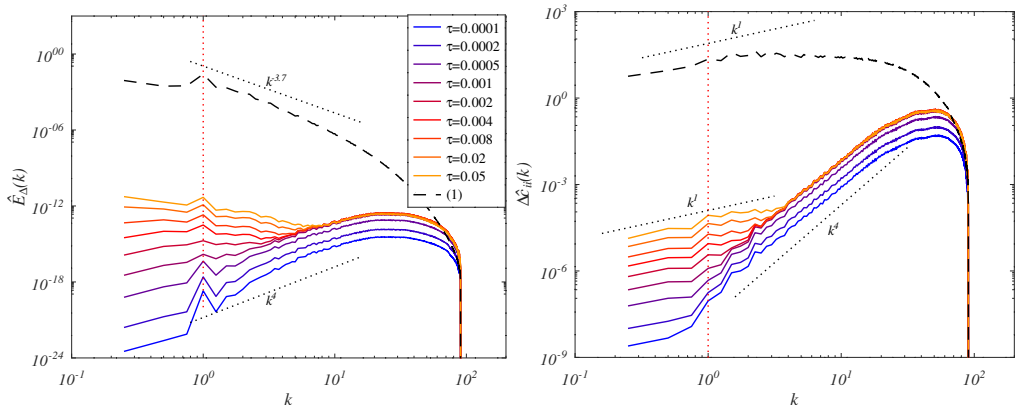


FIGURE 6. Evolution of the uncertainty energy spectrum $\hat{E}_\Delta(k)$ (left panel), and the uncertainty in the conformation tensor trace $\Delta\hat{c}_{ii}(k)$ (right panel) for the reference configuration ($Re = 10^{-2}$, $\beta = 1/2$, $\varepsilon = 0$, $\kappa = 2.5 \times 10^{-5}$, $n = 4$, $Wi = 2$) at very short times (regime (I)). The dashed black lines show the reference energy spectrum $\hat{E}^{(1)}$ and conformation tensor trace $\hat{c}^{(1)}(k)$. The dotted red line indicates the forcing wavenumber $k = 2\pi$.

3.1.4. The spectra of uncertainty

We next investigate how the spectra of the uncertainty evolves. We calculate the energy spectra of Δu_i (denoted \hat{E}_Δ), and the spectra of Δc_{ii} (denoted $\Delta\hat{c}_{ii}$). Figure 6 shows \hat{E}_Δ (left panel) and $\Delta\hat{c}_{ii}$ (right panel) at very early times $\tau \leq 0.05$, covering until nearly the end of regime (I). Figure 7 shows the same for $\tau \in [0.1, 0.6]$, covering regime (II). Figure 8 shows the same at later times $\tau \in [1, 32]$, covering regime (III). In all three figures, the forcing wavenumber is indicated by a vertical dotted red line, and the spectra of the reference field (averaged over 50 time units) is shown with a black dashed line.

At early times (figure 6) the uncertainty energy and uncertainty in the conformation tensor trace are predominantly at high wavenumbers. This is due to the nature of the perturbation, which is imposed via (3.1). At the earliest times, both \hat{E}_Δ and $\Delta\hat{c}_{ii}$ have a slope of k^4 , consistent with the ∇^4 operator used to impose the perturbation. For $\tau \leq 10^{-3}$, there is an increase in \hat{E}_Δ and $\Delta\hat{c}_{ii}$ across all wavenumbers, as the perturbation is applied over a finite time - the characteristic time-scale of the perturbation in (3.1) is 10^{-3} . From the earliest times, there is an almost immediate increase in uncertainty at large scales, and this increase continues after the perturbation has ceased, and spreads across a greater range of wavenumbers with increasing τ . This transfer of uncertainty from small scales to large scales is due to the elliptic constraint of incompressibility: small scale uncertainty localised at one point in space creates uncertainty everywhere, instantly.

At slightly longer times - $\tau \in [0.1, 1]$ (figure 7), there is a reduction in uncertainty at small scales, and the uncertainty at large scales remains roughly constant. This period corresponds to regime (II) as defined above, and the time during which the viscous dissipation of uncertainty dominates polymeric production. We see a slight reduction in \hat{E}_Δ across all scales, and a decrease in $\Delta\hat{c}_{ii}$ at small scales. In this regime the spectra \hat{E}_Δ has a slope of approximately k^{-2} , and $\Delta\hat{c}_{ii}$ has a slope (which matches that of $\hat{c}_{ii}^{(1)}$) of k^1 . After this (regime (III), figure 8), there is exponential growth of \hat{E}_Δ and $\Delta\hat{c}_{ii}$. This exponential growth occurs initially at large scales, whilst diffusion still dominates small scales until $\tau \approx 4$, after which we see exponential growth across all scales. With

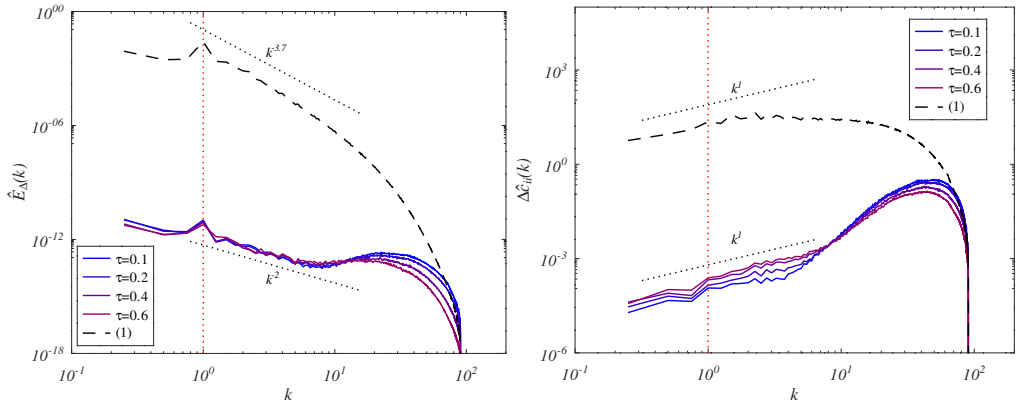


FIGURE 7. Evolution of the uncertainty energy spectrum $\hat{E}_\Delta(k)$ (left panel), and the uncertainty in the conformation tensor trace $\Delta\hat{c}_{ii}(k)$ (right panel) for the reference configuration ($Re = 10^{-2}$, $\beta = 1/2$, $\varepsilon = 0$, $\kappa = 2.5 \times 10^{-5}$, $n = 4$, $Wi = 2$) at short times (regime (II)). The dashed black lines show the reference energy spectrum $\hat{E}^{(1)}$ and conformation tensor trace $\hat{c}^{(1)}(k)$. The dotted red line indicates the forcing wavenumber $k = 2\pi$.

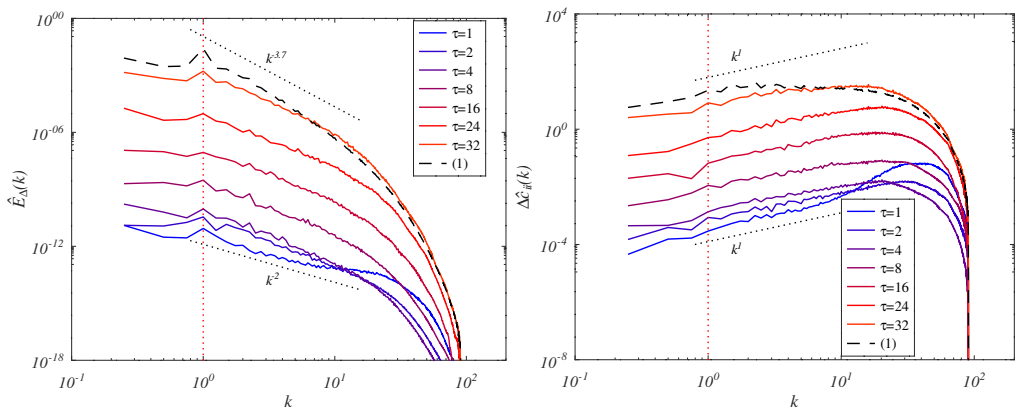


FIGURE 8. The evolution of the uncertainty energy spectrum $\hat{E}_\Delta(k)$ (left panel), and the uncertainty in the conformation tensor trace $\Delta\hat{c}_{ii}(k)$ (right panel) for the reference configuration ($Re = 10^{-2}$, $\beta = 1/2$, $\varepsilon = 0$, $\kappa = 2.5 \times 10^{-5}$, $n = 4$, $Wi = 2$) at longer times (regime (III)). The dashed black lines show the reference energy spectrum $\hat{E}^{(1)}$ and conformation tensor trace $\hat{c}^{(1)}(k)$. The dotted red line indicates the forcing wavenumber $k = 2\pi$.

increasing τ , the slope of \hat{E}_Δ increases towards $k^{-3.5}$, the slope of the reference energy spectra.

In figure 9 we plot the time evolution of individual components of \hat{E}_Δ (left panel) and $\Delta\hat{c}_{ii}$ (right panel). The different regimes of uncertainty evolution are marked with vertical dotted red lines. We denote regime (0) as the timescale over which the perturbation is imposed. For \hat{E}_Δ , the uncertainty at small scales initially grows at a rate proportional to τ^2 , which is consistent with the injection of uncertainty during the imposition of the perturbation for $\tau < \delta_{t0}$. For $\tau > \delta_{t0}$, this growth at small scales ceases. For $\Delta\hat{c}_{ii}$, this early growth at small scales is at a rate proportional to τ . The picture is different at large scales, with \hat{E}_Δ growing proportional to τ^6 , and $\Delta\hat{c}_{ii}$ growing proportional to τ^2 . This growth at large scales continues for $\tau > \delta_{t0}$. We have also performed simulations with $\delta_{t0} = 10^{-5} \ll \delta t = 4 \times 10^{-4}$, where δt is the computational time step. Even in this

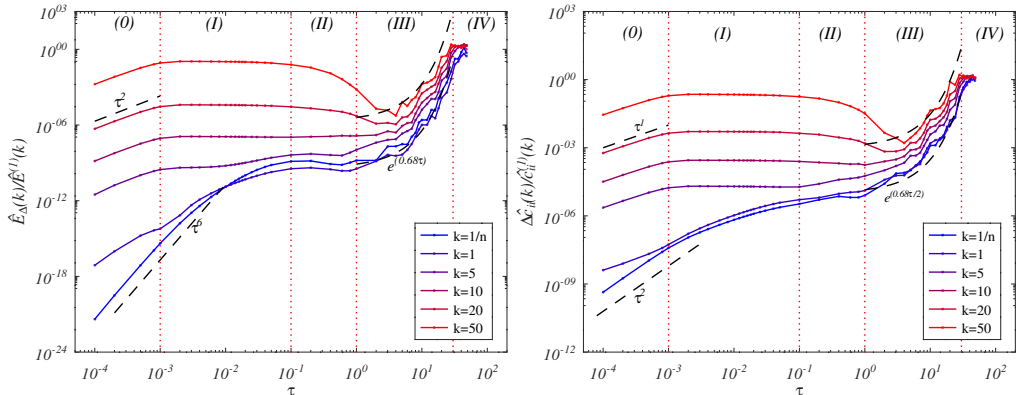


FIGURE 9. The time evolution of components of the uncertainty energy spectra $\hat{E}_\Delta(k)$ (left panel), and the spectra of the uncertainty in conformation tensor trace $\Delta\hat{c}_{ii}(k)$ (right panel), normalised by the reference spectra, for the reference configuration ($Re = 10^{-2}$, $\beta = 1/2$, $\varepsilon = 0$, $Sc = 4 \times 10^6$, $n = 4$, $Wi = 2$).

limit, the same short-time growth rate of τ^6 is observed, and this growth rate persists for the same duration (i.e. it persists until $\tau \gg \delta_{t0}$).

Through regime (I), the uncertainty in both flow and conformation tensor continues to grow at large scales, whilst the uncertainty at small scales is roughly constant. The growth rate decreases with time, as the balance between viscous dissipation and polymeric production changes. By $\tau \approx 0.1$, viscous dissipation of uncertainty becomes greater than polymeric production, and the uncertainty in both flow and conformation tensor decreases at small scales through regime (II). For $\tau > 1$, in regime (III), there is exponential growth of uncertainty in both the flow and conformation tensor, again initially at large scales, and followed by small scales by $\tau \approx 4$. For $\tau > 30$, in regime (IV), the uncertainty saturates at all scales.

We comment here on the short time evolution of uncertainty. If we impose a perturbation on $c_{ij}^{(2)}$ using a Laplacian operator (rather than a hyperviscous operator), we observe qualitatively similar behaviour during regimes (I) and (II). We note that for all perturbations, regimes (III) and (IV) are unchanged; the growth rate in regime (III), and the saturation values in regime (IV), are independent of the perturbation imposed.

3.2. The effect of ε and κ

The sPTT model exhibits shear thinning behaviour, and the extent of this shear thinning increases with increasing nonlinearity ε . To explore the influence of this nonlinearity on the uncertainty dynamics, we run simulations for $\varepsilon \in [0, 10^{-4}, 10^{-3}, 10^{-2}, 10^{-1}]$, with all other parameters matching the reference configuration. For $\varepsilon = 10^{-1}$ the flow remains laminar, and the mean kinetic energy is larger than for $\varepsilon = 0$ by an order of magnitude. The left panel of figure 10 shows the evolution of $\langle E_\Delta \rangle / E_{avg}^{(tot)}$ and $\langle \Gamma_\Delta \rangle / Wi^2$ for $\varepsilon \in [0, 10^{-4}, 10^{-3}, 10^{-2}]$. A similar chaotic flow is observed for all ε in this range, with an exponential growth rate in regime (III) approximately independent of ε . The saturation values of $\langle \Gamma_\Delta \rangle$ and $\langle E_\Delta \rangle$ in regime (IV) are changed to a small extent by the nonlinearity, with larger ε slightly reducing these maximum values; increasing nonlinearity reduces the maximum decorrelation achievable. We also observe some differences in the early time evolution of uncertainty (shown in the inset). For larger ε , the decrease in uncertainty in regime (II) is more pronounced, and occurs across all length scales in both the flow and polymer deformation fields (spectra calculated but not

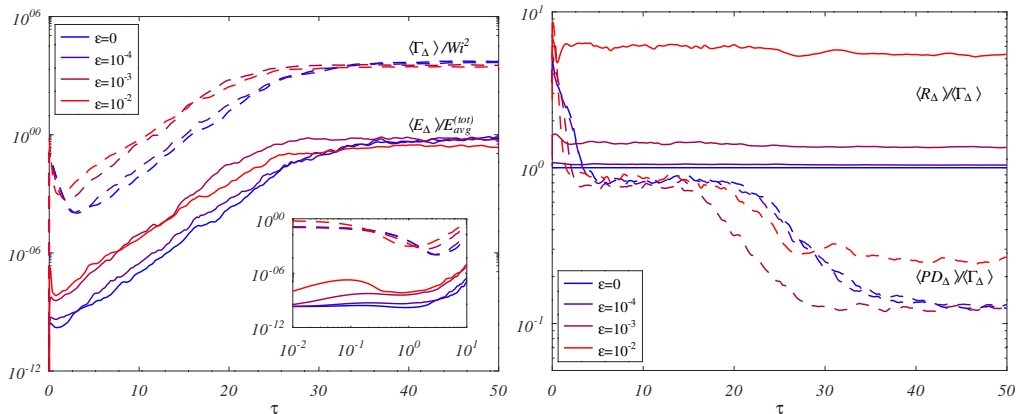


FIGURE 10. Left panel: The evolution of $\langle E_{\Delta} \rangle / E_{avg}^{(tot)}$ and $\langle \Gamma_{\Delta} \rangle / Wi^2$ for a range of ε . Right panel: The evolution of ratios $\langle R_{\Delta} \rangle / \langle \Gamma_{\Delta} \rangle$ and $\langle PD_{\Delta} \rangle / \langle \Gamma_{\Delta} \rangle$. All other parameters match the reference configuration ($Re = 10^{-2}$, $\beta = 1/2$, $\kappa = 2.5 \times 10^{-5}$, $n = 4$, $Wi = 2$).

shown here for brevity). The right panel of figure 10 shows the evolution of $\langle R_{\Delta} \rangle / \langle \Gamma_{\Delta} \rangle$ and $\langle PD_{\Delta} \rangle / \langle \Gamma_{\Delta} \rangle$. For $\varepsilon = 0$, $\langle R_{\Delta} \rangle / \langle \Gamma_{\Delta} \rangle = 1$ by definition. In all cases simulated, $\langle R_{\Delta} \rangle$ remains positive. With increasing nonlinearity, this ratio increases, and develops some temporal variation, although this temporal variation remains small. For $\varepsilon = 10^{-2}$, $\langle R_{\Delta} \rangle / \langle \Gamma_{\Delta} \rangle \approx 8$. During the exponential growth regime (III), the ratio $\langle PD_{\Delta} \rangle / \langle \Gamma_{\Delta} \rangle$ fluctuates, but remains in the range $[0.7, 0.9]$ throughout. For all four values of ε , there is a decrease in $\langle PD_{\Delta} \rangle / \langle \Gamma_{\Delta} \rangle$ as regime (IV) is approached, and the final value of this ratio is larger (approximately 0.3) for $\varepsilon = 10^{-2}$, than for $\varepsilon \leq 10^{-3}$ (approximately 0.15). We note that the ratio of $\langle R_{\Delta} \rangle / \langle PD_{\Delta} \rangle$ increases with increasing ε , suggesting that for a given configuration (Re , Wi , β , κ , n), increasing nonlinearity reduces the relative effects of polymeric diffusivity on the evolution of uncertainty. Not shown, we note that $\langle P_{\Delta} \rangle / \langle D_{\Delta} \rangle - 1$ is dependent on ε . For larger ε , the magnitude of the variation of $\langle P_{\Delta} \rangle / \langle D_{\Delta} \rangle - 1$ in regimes (I) and (II) (shown in the inset of the right panel of figure 4 for $\varepsilon = 0$) increases, and the decrease in $\langle E_{\Delta} \rangle$ observed during regime (II) is more pronounced.

Figure 11 shows snapshots of the conformation tensor field for a range of ε . For smaller ε we see more large scale structures spanning the domain and breaking the cellular structure of the flow. For $\varepsilon = 10^{-2}$, the cellular structure of the flow is much stronger. This is consistent with the larger value of $\langle E_{\Delta} \rangle / E_{avg}^{(tot)}$ obtained for smaller ε in the saturation of uncertainty regime (IV).

Polymeric diffusivity acts to limit the smallest length scales of the polymer deformation field, and we see from (2.15) that the effect of polymeric diffusivity on uncertainty is to reduce it. The left panel of figure 12 shows the evolution of $\langle E_{\Delta} \rangle / E_{avg}^{(tot)}$ and $\langle \Gamma_{\Delta} \rangle / Wi^2$ for $\kappa \in [10^{-4}, 5 \times 10^{-5}, 2.5 \times 10^{-5}]$. The growth rate of uncertainty during regime (III) increases with decreasing κ . At short times, the polymeric diffusivity has a significant influence on the uncertainty. The inset shows the short time evolution of $\langle E_{\Delta} \rangle / E_{avg}^{(tot)}$ and $\langle \Gamma_{\Delta} \rangle / Wi^2$, collapsing when scaled by κ^3 . This dependence on κ is a result of the form of the perturbation: the perturbation imposed generates polymeric deformation difference spectra which scales with k^4 (as in figure 6). Polymeric diffusivity limits the smallest length scales of the polymer deformation field, and consequently the imposed perturbation is smaller for larger κ . The right panel of figure 12 shows the evolution of the terms in (2.15), normalised by $\langle \Gamma_{\Delta} \rangle$, for different κ . The inset shows the early

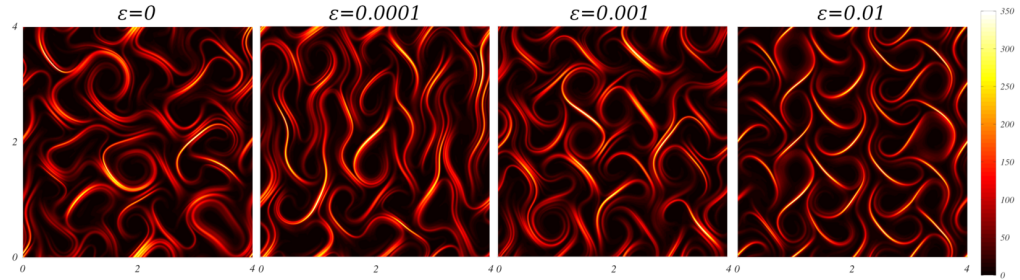


FIGURE 11. Snapshots of the conformation tensor trace field for $\varepsilon \in [0, 10^{-4}, 10^{-3}, 10^{-2}]$. All other parameters match the reference configuration ($Re = 10^{-2}$, $\beta = 1/2$, $\kappa = 2.5 \times 10^{-5}$, $n = 4$, $Wi = 2$).

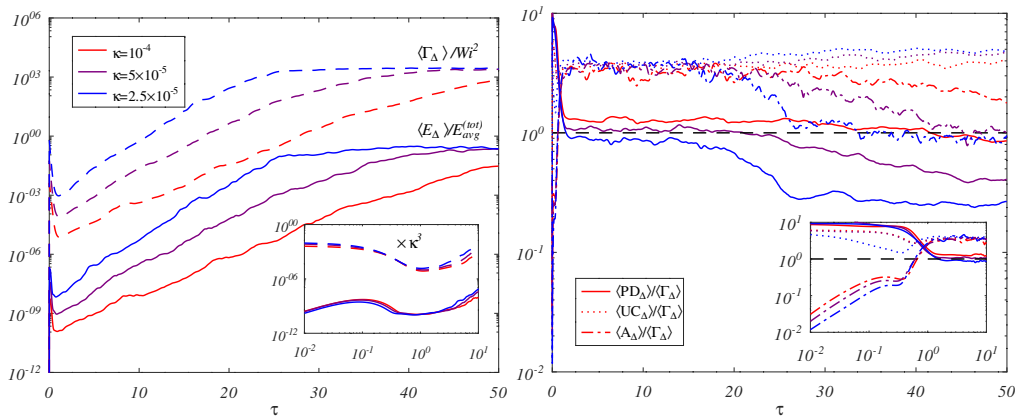


FIGURE 12. Left panel: The evolution of $\langle E_{\Delta} \rangle / E_{avg}^{(tot)}$ and $\langle \Gamma_{\Delta} \rangle / Wi^2$ for different values of κ . Right panel: the evolution of terms in (2.15), normalised by $\langle \Gamma_{\Delta} \rangle$ for different values of κ . All other parameters match the reference configuration ($Re = 10^{-2}$, $\beta = 1/2$, $\varepsilon = 0$, $n = 4$, $Wi = 2$).

time evolution. The relative magnitude of $\langle UC_{1\Delta} \rangle$ and $\langle A_{\Delta} \rangle$ is little changed by κ . At very short times, $\langle PD_{\Delta} \rangle / \langle \Gamma_{\Delta} \rangle$ is independent of κ . During regime (III), $\langle PD_{\Delta} \rangle / \langle \Gamma_{\Delta} \rangle$ is approximately constant, with a value proportional to κ . For all three values of κ , the terms $\langle UC_{1\Delta} \rangle$ and $\langle A_{\Delta} \rangle$ are larger than $\langle PD_{\Delta} \rangle$ during regime (III).

3.3. The influence of Re

We next investigate the influence of Re , keeping all other parameters fixed. The left panel of figure 13 shows the evolution of $\langle E_{\Delta} \rangle / E_{avg}^{(tot)}$ and $\langle \Gamma_{\Delta} \rangle / Wi^2$ for a range $Re \in [10^{-4}, 10^{-3}, 10^{-2}, 10^{-1}, 1]$. The growth rate of uncertainty during regime (III) is shown in the inset, and appears weakly dependent on Re for $Re < 0.1$. For $Re = 1$, the growth rate decreases. The right panel of figure 13 shows the evolution of $\langle I_{\Delta} \rangle$, $\langle D_{\Delta} \rangle$, and $\langle P_{\Delta} \rangle$. The evolution of $|\langle I_{\Delta} \rangle|$ grows in approximately proportion to $\langle E_{\Delta} \rangle$, with the proportionality independent of Re . The magnitudes of $\langle D_{\Delta} \rangle$, and $\langle P_{\Delta} \rangle$ scale with Re^{-1} . The quantities $\langle P_{\Delta} \rangle / \langle D_{\Delta} \rangle - 1$ and $-\langle I_{\Delta} \rangle / \langle D_{\Delta} \rangle$ also scale with Re^{-1} ; this collapse is anticipated provided the average flow is independent of Re , as both $\langle P_{\Delta} \rangle$ and $\langle D_{\Delta} \rangle$ contain Re in the denominator. What is remarkable is that the average ratio of these quantities during

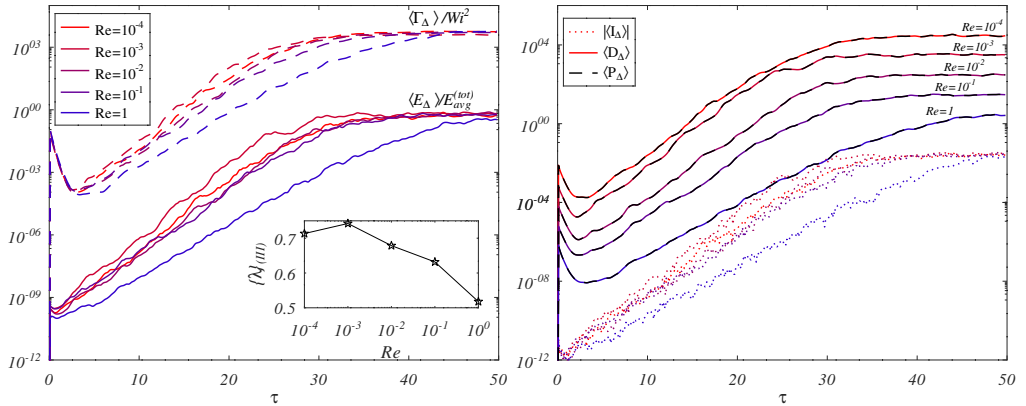


FIGURE 13. Left panel: The evolution of $\langle E_{\Delta} \rangle / E_{avg}^{(tot)}$ and $\langle \Gamma_{\Delta} \rangle / Wi^2$ for a range of Re . All other parameters match the reference configuration ($\beta = 1/2$, $\varepsilon = 0$, $\kappa = 2.5 \times 10^{-5}$, $n = 4$, $Wi = 2$). Inset shows the average growth rate over regime (III). Right panel: The evolution of $\langle I_{\Delta} \rangle$, $\langle D_{\Delta} \rangle$, and $\langle P_{\Delta} \rangle$ for a range of Re .

regime (III) is only weakly dependent on Re . Defining

$$C(Re) = \frac{\{\langle I_{\Delta} \rangle / \langle D_{\Delta} \rangle\}_{(III)}}{\left[\{\langle P_{\Delta} \rangle / \langle D_{\Delta} \rangle\}_{(III)} - 1 \right]}, \quad (3.7)$$

in which $C(Re)$ is a function of Re , we find $C \in [0.11, 0.12, 0.12, 0.14, 0.15]$ for $Re \in [10^{-4}, 10^{-3}, 10^{-2}, 10^{-1}, 1]$. The relative importance of the inertial production of uncertainty is still of the order of 10% even for $Re = 10^{-4}$. How $C(Re)$ approaches zero in the limit $Re \rightarrow 0$ is an interesting question, but one which we leave for future studies. We have also calculated the ratios $\{\langle A_{\Delta} \rangle / \langle R_{\Delta} \rangle\}_{(III)}$ and $\{\langle UC1_{\Delta} \rangle / \langle R_{\Delta} \rangle\}_{(III)}$ and find that both ratios are independent of Re .

Figure 14 shows snapshots of the conformation tensor trace field for three values of Re . Note that in these snapshots, structures similar to the “narwhal” or “arrowhead” structures recently identified as exact travelling wave solutions (Page *et al.* 2020; Morozov 2022) are visible for both $Re = 10^{-4}$ and $Re = 1$. These larger scale structures spanning the domain and breaking the cellular structure of the flow are present *intermittently* at all Re investigated, but are present for a greater proportion of the time at larger Re . We also note that the occurrence of these structures is less frequent at larger ε : we do not observe them at all for simulations with $\varepsilon = 10^{-2}$.

We next assess the influence of Re on the spectra of uncertainty, following the same analysis as above for the reference configuration. The results are shown in figure 15. From figure 13, we have observed the evolution of uncertainty in regime (III) is only weakly dependent on Re , and here we are interested in how the inertial terms influence the early stages of uncertainty growth. At short times, for all $Re \in [10^{-4}, 1]$ we see the same growth rates: at the largest scales, \hat{E}_{Δ} grows with τ^6 , and this growth rate persists for some time after the imposition of the perturbation. At the smallest scales, \hat{E}_{Δ} grows with τ^2 during the imposition of the perturbation, after which it plateaus, before diffusive effects begin to reduce uncertainty. Although the growth rate is independent of Re , the magnitude of \hat{E}_{Δ} at small k scales approximately with Re^{-2} . This can be seen in the inset of the left panel of figure 15, which shows the early stages of the evolution of $Re^2 \hat{E}_{\Delta}$. There appears to be a maximum uncertainty in the large scales during regime (II). For smaller Re , the growth proportional to τ^6 persists for a shorter time. For all $Re \leq 1$,

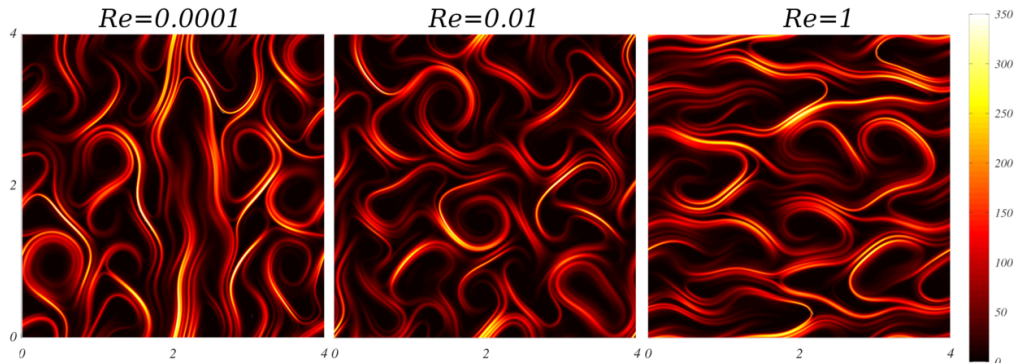


FIGURE 14. Snapshots of the conformation tensor trace field for $Re \in [10^{-4}, 10^{-2}, 1]$. All other parameters match the reference configuration ($\beta = 1/2$, $\varepsilon = 0$, $\kappa = 2.5 \times 10^{-5}$, $n = 4$, $Wi = 2$).

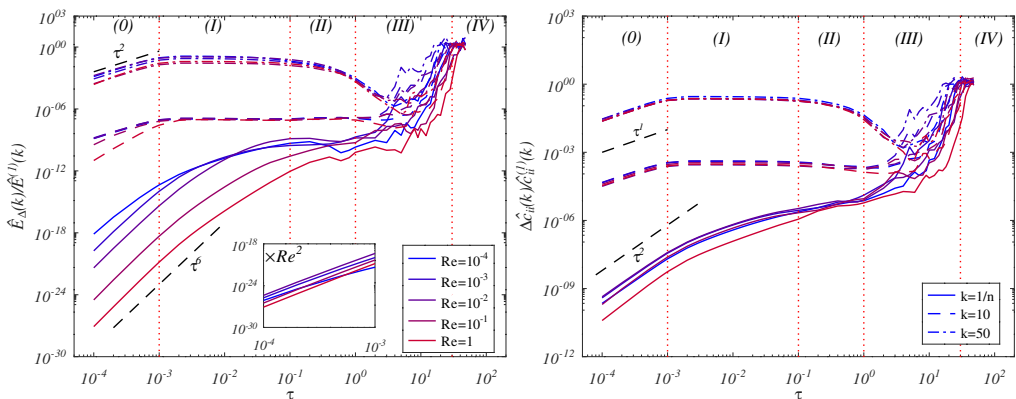


FIGURE 15. The time evolution of components of the uncertainty energy spectra $\hat{E}_\Delta(k)$ (left panel), and the spectra of the uncertainty in conformation tensor trace $\Delta \hat{c}_{ii}(k)$ (right panel), normalised by the reference spectra, for different values of Re . The inset of the left panel shows components of $\hat{E}_\Delta(k)$ scaled by Re^2 . The line styles correspond to different wavenumbers, with $k = 1/n$ - solid lines, $k = 10$ - dashed lines, and $k = 50$ - dash-dot lines. All other parameters match the reference configuration ($\beta = 1/2$, $\varepsilon = 0$, $\kappa = 2.5 \times 10^{-5}$, $n = 4$, $Wi = 2$).

the low wavenumber components of \hat{E}_Δ reach a similar magnitude during the transition from regime (I) to regime (II), after which the evolution during the exponential growth regime (III) tracks approximately the same course. For $Re = 10$, the evolution of the large scales of uncertainty is qualitatively similar, but with smaller magnitudes and lower growth rates during the exponential regime (III).

3.4. The effect of increasing Wi

We next investigate the influence of elasticity on the evolution of uncertainty. Following the observation in § 3.2 that for a given configuration, increased nonlinearity reduces the relative influence of polymeric diffusivity on the evolution of uncertainty, in this section, we take a base configuration with $\varepsilon = 10^{-2}$ ($Re = 10^{-2}$, $\beta = 1/2$, $\varepsilon = 10^{-2}$, $\kappa = 2.5 \times 10^{-5}$, $n = 4$), and vary Wi . Relative to the case with $\varepsilon = 0$, we expect this to allow us to reach larger Wi without the effects of polymeric diffusivity masking the nature of how the uncertainty evolution varies with Wi . Figure 16 shows snapshots of the vorticity field (upper panel) and normalised conformation tensor trace $c_{ii}^{(1)}/Wi$ (lower panel) for different values of Wi . For $Wi = 0.5$, the flow is steady, the flow pattern is periodic on the

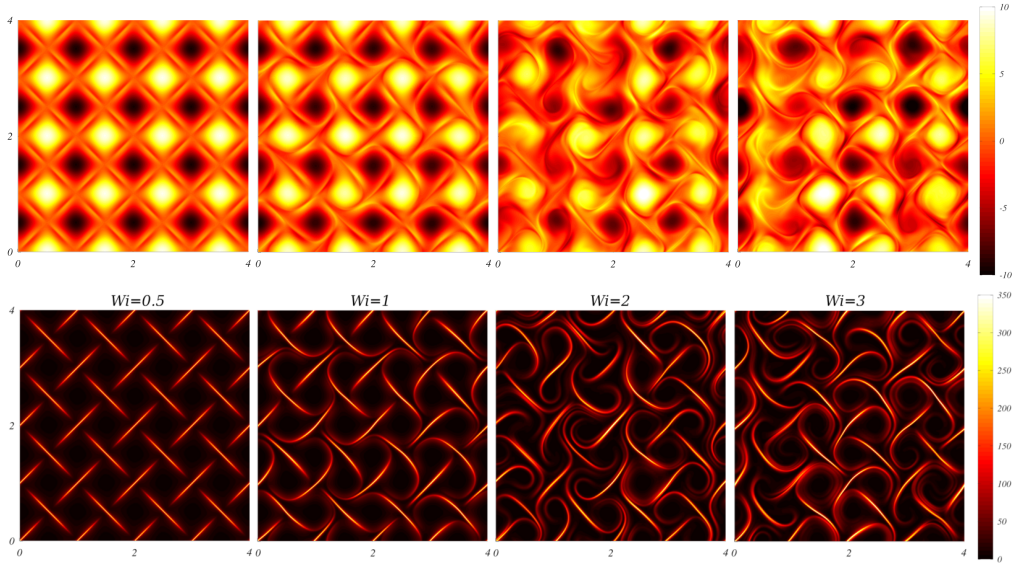


FIGURE 16. Snapshots of the vorticity field (top), and normalised conformation tensor trace ($c_{ii}^{(1)}/Wi$) (bottom) for increasing Wi . Other parameters are ($Re = 10^{-2}$, $\beta = 1/2$, $\varepsilon = 10^{-2}$, $\kappa = 2.5 \times 10^{-5}$, $n = 4$)

scale of the forcing, and in a laminar regime. With increasing Wi there is a symmetry breaking as the thin regions of high polymer deformation between cells interact with stagnation points and are swept laterally. Figure 17 shows the evolution of $\langle E_{\Delta} \rangle / E_{avg}^{(tot)}$ and $\langle \Gamma_{\Delta} \rangle / Wi^2$ for a range of $Wi \in [0.5, 3]$. To reach larger Wi , we require either a finer resolution, or larger values polymeric diffusivity. The former will increase computational costs to a level beyond our resources for this work (doubling resolution increases costs by a factor of > 8). We show in the right panel of figure 17 the evolution of $\langle E_{\Delta} \rangle / E_{avg}^{(tot)}$ and $\langle \Gamma_{\Delta} \rangle / Wi^2$ for a range of $Wi \in [1, 20]$, with polymeric diffusivity increased to $\kappa = 10^{-4}$. This increase in κ permits stable simulations at larger Wi , but it is likely the dynamics of the flow are influenced by the polymeric diffusivity, particularly at larger elasticities. For smaller Wi we see a sub-linear increase in the growth rate of uncertainty during the exponential regime (insets of both panels of figure 17). The dashed-black lines in both insets are linear in $Wi^{0.7}$, and for $\kappa = 2.5 \times 10^{-5}$ in the left panel, there is a reasonable fit, suggesting the growth rate of uncertainty scales approximately with $Wi^{0.7}$. Acknowledging that Lyapunov dimension and Lyapunov exponent are different, we note that the Lyapunov dimension obtained by Plan *et al.* (2017) was given in the form CWi^{α} , with $\alpha \approx 0.7$. At large Wi (right panel of figure 17) this increase in $\{\lambda\}_{(III)}$ ceases, and for $\kappa = 10^{-4}$ and $Wi \geq 8$, the growth rate of uncertainty is roughly constant with further increases in Wi . We postulate that this limit is a consequence of the larger polymeric diffusivity, which acts to reduce uncertainty growth. For the simulations with larger κ , we observe a much more significant decrease of uncertainty at low Wi during regime (II); in the right panel of figure 17, $\langle E_{\Delta} \rangle / E_{avg}^{(tot)}$ decreases significantly with decreasing Wi during the early stages when polymeric diffusion dominates the uncertainty evolution. We note here that the rapid transfer of uncertainty across scales during regime (I) occurs for all Wi investigated (even those at low Wi in the laminar regime), and the growth rate or large scale uncertainty with τ^6 in this regime holds across the range of Wi .

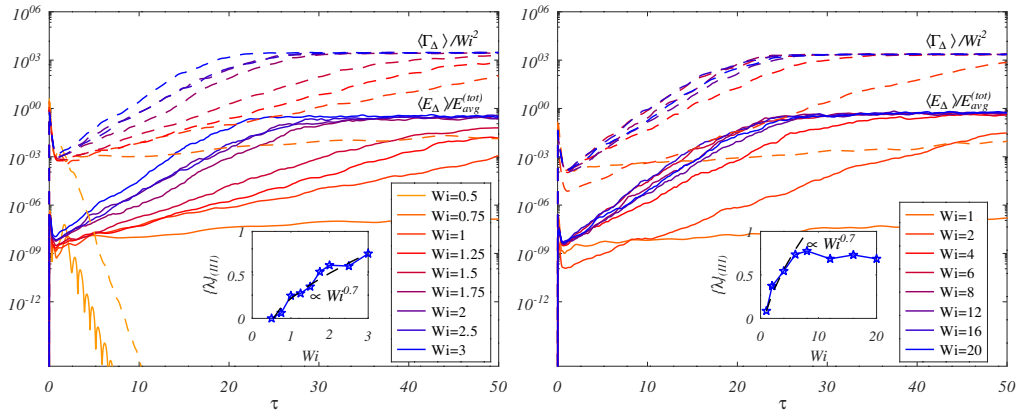


FIGURE 17. Time evolution of $\langle E_{\Delta} \rangle / E_{avg}^{(tot)}$ and $\langle \Gamma_{\Delta} \rangle / Wi^2$, with increasing Wi . In the left panel, other parameters are ($Re = 10^{-2}$, $\beta = 1/2$, $\varepsilon = 10^{-2}$, $\kappa = 2.5 \times 10^{-5}$, $n = 4$). In the right panel, the polymeric diffusivity is increased to $\kappa = 10^{-4}$.

3.5. The effect of increasing domain size n

Finally, we explore the influence of the domain size. We have observed in regime (I) rapid transfer of uncertainty across scales, and with the configuration used in this work, it is interesting to explore how uncertainty evolves differently as the domain size is changed. Note, that our non-dimensionalisation is based on the forcing, and not on any large scale flow features which may develop. An alternative non-dimensionalisation is possible, based on a fixed (unit) domain size, as was used in Plan *et al.* (2017). In that work they estimated the Lyapunov dimension for two difference forcing wavelengths, and obtained a scaling with Wi which was independent of the forcing scale. Denoting the dimensionless quantities based on the domain size with a subscript n , we can express the relationship $Re_n = nRe$, and $Wi_n = Wi/n$. If we non-dimensionalise based on the domain size, for fixed fluid transport properties (i.e. viscosity, relaxation times) and forcing magnitude, the Reynolds number would increase with domain size, and the Weissenberg number would scale with the inverse of domain size. Defining the Elasticity number as $El = Wi/Re$, we see the domain size based elasticity number El_n scales with $1/n^2$. We conduct simulations all with the same (unit) forcing wavelength, for a range of domain sizes $n \in [2, 16]$, and for three configurations: 1) with all other parameters matching the reference configuration ($Re = 10^{-2}$, $\beta = 1/2$, $\varepsilon = 0$, $\kappa = 2.5 \times 10^{-5}$, $Wi = 2$); 2) using the sPTT model ($Re = 10^{-2}$, $\beta = 1/2$, $\varepsilon = 10^{-2}$, $\kappa = 2.5 \times 10^{-5}$, $Wi = 2$); and 3) with the sPTT model and increased polymeric diffusivity ($Re = 10^{-2}$, $\beta = 1/2$, $\varepsilon = 10^{-2}$, $\kappa = 10^{-4}$, $Wi = 2$). Note that whilst the mean kinetic energy is independent of n , high-energy intermittent events increase with increasing n , and consequently for $n > 10$, we use a smaller timestep of $\delta t = 2 \times 10^{-4}$.

The left panel figure 18 shows the evolution of $\langle E_{\Delta} \rangle / E_{avg}^{(tot)}$ and $\langle \Gamma_{\Delta} \rangle / Wi^2$ with increasing domain size n . All other parameters match configuration 2) described above ($Re = 10^{-2}$, $\beta = 1/2$, $\varepsilon = 10^{-2}$, $\kappa = 2.5 \times 10^{-5}$, $Wi = 2$). In the right panel, the results are plotted against $\tau \ln(n^{0.5})$. In the left panel, it is clear that increasing the maximum length scales of the flow results in a faster growth of uncertainty during regime (III). The collapse of the curves in the right panel of figure 18 shows this increased growth rate follows a trend of approximately $\ln(n^{0.5})$. Our numerical experiments in which we increase n for a fixed forcing strength may be re-framed as a set in which we increase $El_n^{-1/2}$ whilst co-varying Re_n and Wi_n ; we are effectively moving from (at small n) a

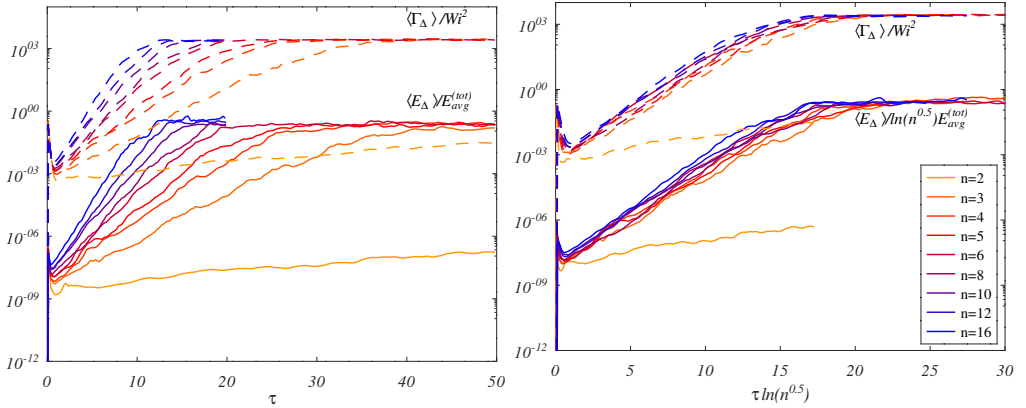


FIGURE 18. Time evolution of $\langle E_{\Delta} \rangle / E_{avg}^{(tot)}$ and $\langle \Gamma_{\Delta} \rangle / Wi^2$ with increasing domain size n . Other parameters are ($Re = 10^{-2}$, $\beta = 1/2$, $\varepsilon = 10^{-2}$, $\kappa = 2.5 \times 10^{-5}$, $Wi = 2$). On the left panel, τ has been rescaled by $\ln(n^{0.5})$.

high- El_n regime where inertial effects are negligible, to (at large n) a low El_n regime in which inertial effects play an increasing role.

We denote the average growth rate during regime (III) as $\{\lambda\}_{(III)}$, and this is plotted against n in figure 19, for several parameter configurations. For the cases with $\varepsilon = 10^{-2}$ (red and black lines), we see that $\{\lambda\}_{(III)}$ scales with $0.5 \ln(n)$ over the range $n \in [4, 16]$. For small n , the growth rate drops below this. For the reference configuration (blue lines/symbols) the growth rate follows this trend up to $n = 6$, and for larger n drops below this trend. For the configuration with $\varepsilon = 0.01$ and an increased $\kappa = 10^{-4}$, a growth rate is lower (due to the effect of polymeric diffusivity to reduce uncertainty growth), but the variation with n still follows the logarithmic trend. For the configuration with increased polymeric diffusivity ($Re = 10^{-2}$, $\beta = 1/2$, $\varepsilon = 0.01$, $\kappa = 10^{-4}$, $Wi = 2$), we can obtain converged results with a resolution of $(64n)^2$ modes, allowing us to reach larger domain sizes at reasonable computational costs. For $n = 32$, the results deviate from the $0.5 \ln(n)$ scaling. The inset of figure 19 shows the variation of $\left\{ Wi^2 \langle E_{\Delta} \rangle / E_{avg}^{(tot)} \langle \Gamma_{\Delta} \rangle \right\}_{(III)}$ with n for the three different configurations. In the Oldroyd B limit, this quantity represents the ratio of uncertainty in kinetic energy to that in elastic energy, and we see for all three configurations, this quantity increases with increasing domain size. This is despite the average energies of the reference field being independent of domain size.

It is known that in two-dimensional inertial turbulence, large scale condensates develop (see e.g. Chertkov *et al.* (2007); Svirsky *et al.* (2023)) in finite domains, due to the inverse energy cascade and accumulation of energy at the largest scales. To our knowledge, such condensates have not been investigated in two-dimensional viscoelastic turbulence, although their existence may be expected settings with out-of-equilibrium forcing. The inverse cascade in two-dimensional (inertial, Newtonian) turbulence arises as a consequence of the additional constraint on the conservation of (squared) vorticity (Svirsky & Frishman 2024). The addition of polymers provides a mechanism which can draw energy from large to small scales, weakening or reversing the cascade depending on the relative balance of inertial and elastic effects (Gillissen 2019). The right panel of figure 19 shows the energy spectra of the reference field for different domain sizes n . We see that there is energy below the forcing wavenumber, as in the simulations of Plan *et al.* (2017). In our simulations the energy spectra below the forcing wavenumber scales with $k^{-\alpha}$ for an $\alpha > 1$; there must be *some* transfer of energy from smaller

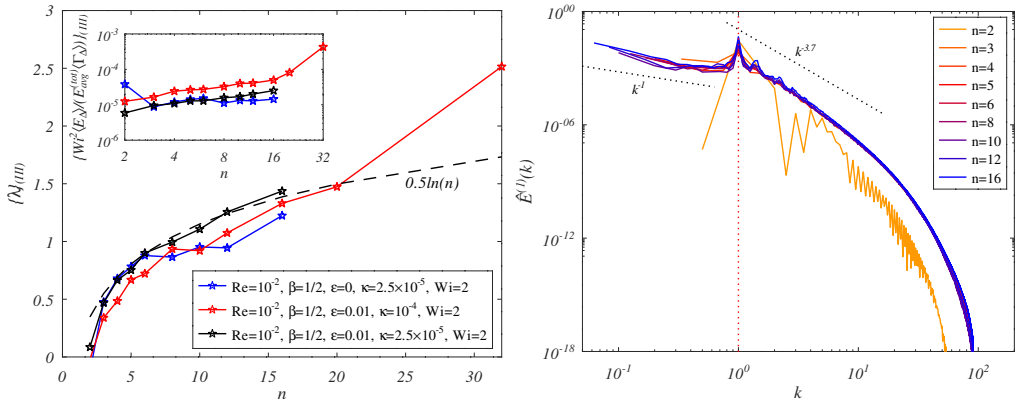


FIGURE 19. Left panel: The variation of the growth rate $\{\lambda\}_{(III)}$ with increasing domain size n , for three different configurations. The dashed line corresponds to $0.5 \ln n$. The inset shows the $\{Wi^2 \langle E_\Delta \rangle / E_{avg}^{(tot)} \langle \Gamma_\Delta \rangle\}_{(III)}$. Right panel: the energy spectra of the reference field for different values of n . All other parameters match the reference configuration ($Re = 10^{-2}$, $\beta = 1/2$, $\varepsilon = 0$, $\kappa = 2.5 \times 10^{-5}$, $Wi = 2$).

to large scales. Furthermore, given the spectra above the forcing wavenumber closely match for all $n \geq 3$, we postulate that it is the large scale flow structures which drive the increase in the rate of uncertainty growth with increasing domain size. Figure 20 shows snapshots of the conformation tensor trace for increasing domain sizes. We see that for $n = 2$, the flow is laminar. With increasing domain size, there are increasing regions exhibiting the arrowhead-like flow structures (Page *et al.* 2020), and increasingly large scale patterns in the polymer deformation. A consequence of the rapid transfer of uncertainty across scales is that if one region of the flow has characteristics which result in a faster uncertainty growth, this will be propagated throughout the domain increasing the uncertainty growth rate everywhere. In figure 20 for $n = 16$, we see some form of large scale structure consisting of alternating regions of arrowhead structures and cellular flow. Understanding the formation and structure of such condensates may provide further insight into the dynamics of elastic turbulence, but such investigations via numerical simulations become prohibitively expensive, and are left for future work. Note that when inspecting the conformation tensor trace fields for the case with sPTT nonlinearity $\varepsilon = 10^{-2}$, we observe large scale patterns spanning the domain, but we do not observe the formation of arrowhead-like structures.

We next consider the terms in (2.8) and (2.15) for varying n . The left panel of figure 21 shows the individual terms in (2.8) for increasing n , plotted against $\tau \ln(n^{0.5})$. The same collapse is observed as in $\langle E_\Delta \rangle / E_{avg}^{(tot)}$ and $\langle \Gamma_\Delta \rangle / Wi^2$ in figure 18. The inset shows the averages during regime (III) of ratios of these terms. Both quantities $\langle I_\Delta \rangle / \langle D_\Delta \rangle$, which represents the ratio of inertial production to viscous dissipation of uncertainty, and $\langle P_\Delta \rangle / \langle D_\Delta \rangle - 1$, which indicates whether polymeric production of uncertainty outweighs viscous dissipation, increase with increasing n , and this increase is roughly linear. However, the ratio $\langle I_\Delta \rangle / (\langle P_\Delta \rangle - \langle D_\Delta \rangle)$ decreases with increasing n , implying the relative influence of inertial effects on uncertainty growth decreases with increasing n .

The right panel of figure 21 shows the evolution of the ratio $\langle R_\Delta \rangle / \langle PD_\Delta \rangle$, plotted against $\tau \ln(n^{0.5})$. At short times, polymeric dissipation of uncertainty dominates in (2.15), and we see this in the inset with small values of $\langle R_\Delta \rangle / \langle PD_\Delta \rangle$ at early times.

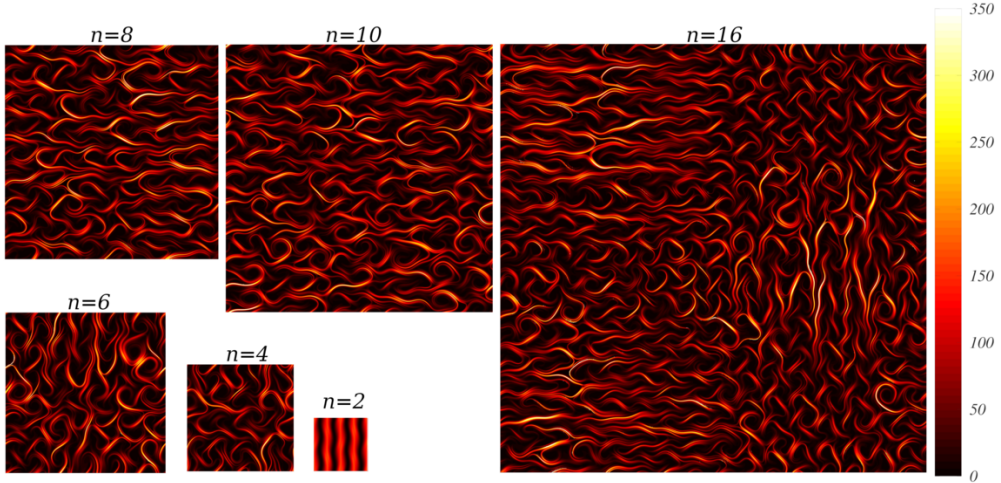


FIGURE 20. Snapshots of the normalised conformation tensor trace ($c_{ii}^{(1)}/Wi$) for increasing n . All other parameters match the reference configuration ($Re = 10^{-2}$, $\beta = 1/2$, $\varepsilon = 0$, $\kappa = 2.5 \times 10^{-5}$, $Wi = 2$).

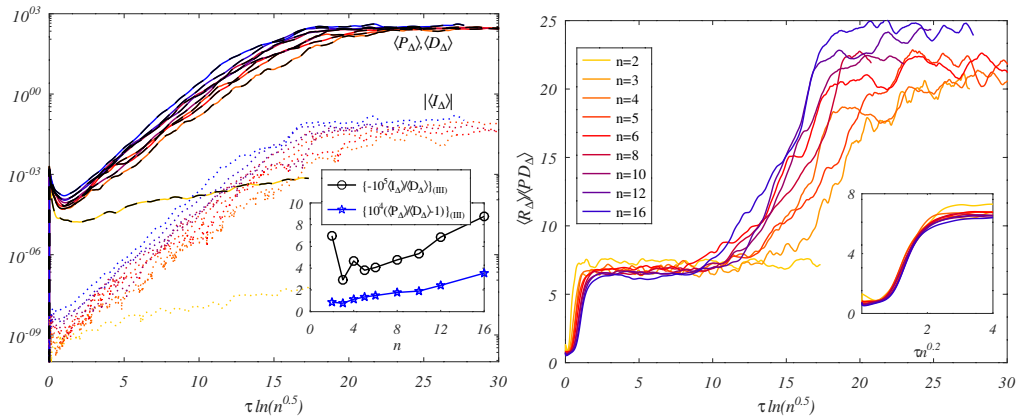


FIGURE 21. Left panel: The time evolution of terms in (2.8) contributing to the evolution of $d\langle E_{\Delta}\rangle/dt$ for a range of domain sizes n . Time is scaled by $0.5 \ln n$. The inset shows the variation of ratios of these terms with n . Right panel: The time evolution of the ratio $\langle R_{\Delta}\rangle/\langle PD_{\Delta}\rangle$, with time scaled by $0.5 \ln n$. The inset shows the short time evolution of this ratio, which collapses with time scaled by $n^{0.2}$. Other parameters are ($Re = 10^{-2}$, $\beta = 1/2$, $\varepsilon = 10^{-2}$, $\kappa = 2.5 \times 10^{-5}$, $Wi = 2$).

Note that we have plotted the data in the inset against $\tau n^{0.2}$ and the early time evolution of $\langle R_{\Delta}\rangle/\langle PD_{\Delta}\rangle$ collapses under this scaling. At the start of regime (III), there is an increase in $\langle R_{\Delta}\rangle/\langle PD_{\Delta}\rangle$ to approximately 6.5, a value that is roughly independent of n , and persists through the exponential regime (III), before increasing further as a saturation of uncertainty is reached. In the left panel of figure 22 we plot the evolution of $\langle A_{\Delta}\rangle/\langle \Gamma_{\Delta}\rangle$. The collapse with $\ln(n^{0.5})$ still holds during regime (III), whilst (not shown), the collapse with $n^{0.2}$ observed for $\langle R_{\Delta}\rangle/\langle PD_{\Delta}\rangle$ holds. At late times, into regime (IV), for all n , $\langle A_{\Delta}\rangle/\langle \Gamma_{\Delta}\rangle$ tends towards the same value just below unity. During regime (III), the average value of $\langle A_{\Delta}\rangle/\langle \Gamma_{\Delta}\rangle$ (plotted in the inset) increases with increasing domain size. We see the same trend for the reference configuration with $\varepsilon = 0$ (blue lines in the inset), but with lower magnitude. The right panel of figure 22 shows the evolution of

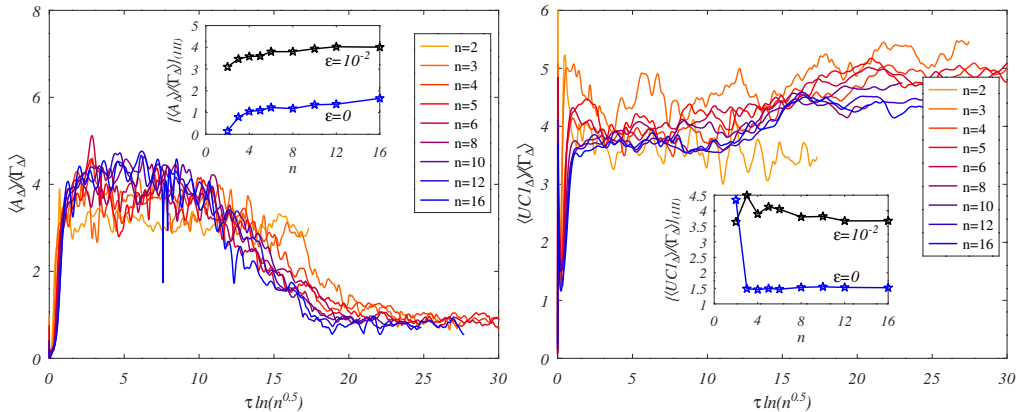


FIGURE 22. The time evolution of terms in (2.15) contributing to the evolution of $\langle \Gamma_\Delta \rangle$. The left panel shows the evolution of the ratio $\langle A_\Delta \rangle / \langle \Gamma_\Delta \rangle$. The right panel shows the evolution of the ratio $\langle UC1_\Delta \rangle / \langle \Gamma_\Delta \rangle$. In both cases, time is scaled by $0.5 \ln n$. The insets show the average values of these ratios over the period of exponential growth. Other parameters are $(Re = 10^{-2}, \beta = 1/2, \varepsilon = 10^{-2}, \kappa = 2.5 \times 10^{-5}, Wi = 2)$.

$\langle UC1_\Delta \rangle / \langle \Gamma_\Delta \rangle$. This ratio appears to be roughly independent of n during regime (III). We know from (2.17) that $\langle UC1_\Delta \rangle$ depends on the relative orientation of the conformation tensor difference with the reference flow field, and the independence of $\langle UC1_\Delta \rangle / \langle \Gamma_\Delta \rangle$ with n suggests changes in the domain size are not changing this orientation. We also note that for all three configurations for which we have conducted the investigation on increasing n , the magnitudes of both $\langle R_\Delta \rangle / \langle \Gamma_\Delta \rangle$ and $\langle PD_\Delta \rangle / \langle \Gamma_\Delta \rangle$ are independent of n during regime (III). The changes we see in growth rate with increasing n appear to be driven by increases in the production of uncertainty via polymeric advection, which couples uncertainty across scales, and corresponding increases in inertial and polymeric production terms in the equation governing the evolution of $\langle E_\Delta \rangle$.

4. Conclusions

In this work we have investigated the dynamics of uncertainty in elastic turbulence. Inspection of the evolution equations for uncertainty provides insight, showing a) that uncertainty in the polymeric deformation field can evolve into uncertainty in both flow and polymer fields, and hence for a chaotic flow exhibiting sensitivity to initial conditions, we would expect small perturbations or uncertainties inherent in polymer orientations to grow in finite time, with implications for the accuracy and repeatability of numerical and laboratory experiments. The growth of uncertainty depends on the relative alignments of the reference flow, the reference conformation tensor, the uncertainty in the flow and the uncertainty in the conformation tensor. The growth of uncertainty in kinetic energy is determined primarily by the balance of viscous dissipation and polymeric production, whilst the growth of uncertainty in elastic energy is primarily controlled by the balance of production due to polymer advection, stretching and rotation, against polymer relaxation and polymeric diffusivity, with the latter two effects always acting to reduce uncertainty.

We identify several regimes of evolution of uncertainty.

(I) At very short times, a transfer of uncertainty across scales, with rapid growth of uncertainty in the flow and polymer deformation at large scales. Uncertainty at any point instantly generates uncertainty everywhere, as a consequence of the elliptic nature of the incompressibility constraint. Over a range of Re , this transfer

of uncertainty from very small to very large scales approximately with Re^{-2} . In this regime uncertainty in the kinetic energy grows with time to the power of 6 for large scales, and this growth rate appears to be independent of Re , Wi , polymeric diffusivity, the degree of non-linearity in the sPTT model, and the domain size.

- (II) At short times, of the order of one dimensionless time unit, a reduction in uncertainty, predominantly at small scales, but in some configurations across all scales, due to viscous and diffusive effects.
- (III) At moderate times, of the order of one to 30 dimensionless time units, exponential growth of uncertainty across all scales. In the elastic turbulence regime, this growth rate decreases slightly with increasing Reynolds number, increases approximately with $Wi^{0.7}$, and increases with the logarithm of the square root of the maximum length scale. The growth rate decreases with increasing polymeric diffusivity, and is largely independent of the degree of nonlinearity in the sPTT model, within the range of nonlinearity which results in elastic turbulence. This regime is characterised by a slight rotation of the uncertainty in the polymeric deformation relative to the reference polymeric deformation, but the average rotation remains approximately constant throughout the regime, even as the magnitude of the uncertainty increases by six orders.
- (IV) At late times, uncertainty saturates. In general, the maximum uncertainty in the kinetic energy, normalised by the total energy, is unity. For flows with a constant forcing, there is a limit to the extent to which the flows can decorrelate, and in the cellularly-forced elastic turbulence setting, this limit appears to be approximately 0.3.

At short times, in particular in regime (II), the uncertainty evolution is influenced by the nature of the initial uncertainty, but the growth rate in regime (III) is independent of the initial uncertainty: it is a function purely of the reference flow state.

The observation of rapid transfer of uncertainty across scales raises questions about closure models (analogous to large eddy simulation for inertial turbulence) for elastic turbulence. If uncertainty at the small scales can completely destabilise the trajectory of a flow across all scales, then any closure models which make assumptions about the flow at unresolved scales must somehow account for this. The observation also supports previous findings by Gupta & Vincenzi (2019); Yerasi *et al.* (2024), and highlights the need to care in numerical simulations of elastic turbulence, as numerical errors or inaccuracies may significantly alter the dynamics at large scales.

The approach taken in this study is new to viscoelastic flows, and there are many aspects we would like to investigate which are beyond the scope of the present paper. In particular, exploring the behaviour of uncertainty at extremely high elasticities, negligible polymeric diffusivities, and extremely large domain sizes would provide further insight, although such investigations require a finer resolution and will result in significantly increased computational costs. The formation of condensates in settings where the maximum length scale is much larger than the forcing scale is a topic which has received little attention in the context of viscoelastic flows, but understanding this behaviour may have implications for the development of closure models for elastic turbulence. Finally, we comment that the theory developed herein could equally be applied to flows with inertia, and a further study of three-dimensional elasto-inertial turbulence is planned.

Acknowledgements

JK is funded by the Royal Society via a University Research Fellowship (URF\R1\221290). We would like to acknowledge the assistance given by Research IT and the use of the Computational Shared Facility at the University of Manchester.

Appendix A. Environmental Impact of simulations

Numerical simulations of the Navier-Stokes equations are computationally intensive, and have an associated carbon footprint. In our field this is rarely discussed or reported, but in the interests of sustainable research, a greater awareness of the environmental cost of simulations is essential. To this end, here we summarise the carbon footprint of simulations used in this study, with calculations performed using the Green Algorithms calculator (Lannelongue *et al.* 2021). All simulations were run on the Computational Shared Facility at the University of Manchester. For configurations with $n = 4$ (at a resolution of $(128n)^2$ modes), a set of simulations (precursor and 10 runs to obtain ensemble averages) required approximately 48 hours on 64 cores of an AMD EPYC Genoa 9634 CPU, with a carbon footprint of approximately 15.6kgCO₂e. Larger simulations were run on up to 168 cores, with the longest run time 360 hours, and a carbon footprint of approximately 180.4kgCO₂e. A small number of large simulations were run on Intel Xeon Gold 6130 CPUs, using up to 1024 cores, with a maximum run time of 120 hours, and the largest simulation having emissions of 454.7kgCO₂e. The combined carbon footprint of *all* simulations used in this work was approximately 8.9×10^3 kgCO₂e. This estimate does not include the cost of post-processing and data analysis.

REFERENCES

- BELL, JOHN B., NONAKA, ANDREW, GARCIA, ALEJANDRO L. & EYINK, GREGORY 2022 Thermal fluctuations in the dissipation range of homogeneous isotropic turbulence. *Journal of Fluid Mechanics* **939**, A12.
- BENEITEZ, MIGUEL, PAGE, JACOB & KERSWELL, RICH R. 2023 Polymer diffusive instability leading to elastic turbulence in plane couette flow. *Phys. Rev. Fluids* **8**, L101901.
- BERTI, S., BISTAGNINO, A., BOFFETTA, G., CELANI, A. & MUSACCHIO, S. 2008 Two-dimensional elastic turbulence. *Phys. Rev. E* **77**, 055306.
- BERTI, S. & BOFFETTA, G. 2010 Elastic waves and transition to elastic turbulence in a two-dimensional viscoelastic kolmogorov flow. *Phys. Rev. E* **82**, 036314.
- BOFFETTA, G., CELANI, A., MAZZINO, A., PULIAFITO, A. & VERGASSOLA, M. 2005 The viscoelastic kolmogorov flow: eddy viscosity and linear stability. *Journal of Fluid Mechanics* **523**, 161–170.
- BROWNE, CHRISTOPHER A. & DATTA, SUJIT S. 2024 Harnessing elastic instabilities for enhanced mixing and reaction kinetics in porous media. *Proceedings of the National Academy of Sciences* **121** (29), e2320962121.
- BURNS, KEATON J., VASIL, GEOFFREY M., OISHI, JEFFREY S., LECOANET, DANIEL & BROWN, BENJAMIN P. 2020 Dedalus: A flexible framework for numerical simulations with spectral methods. *Physical Review Research* **2** (2), 023068.
- CHERTKOV, M., CONNAUGHTON, C., KOLOKOLOV, I. & LEBEDEV, V. 2007 Dynamics of energy condensation in two-dimensional turbulence. *Phys. Rev. Lett.* **99**, 084501.
- COUCHMAN, MILES M.P., BENEITEZ, MIGUEL, PAGE, JACOB & KERSWELL, RICH R. 2024 Inertial enhancement of the polymer diffusive instability. *Journal of Fluid Mechanics* **981**, A2.
- DATTA, SUJIT S., ARDEKANI, AREZOO M., ARRATIA, PAULO E., BERIS, ANTONY N., BISCHOFBERGER, IRMGARD, MCKINLEY, GARETH H., EGGERS, JENS G., LÓPEZ-AGUILAR, J. ESTEBAN, FIELDING, SUZANNE M., FRISHMAN, ANNA, GRAHAM, MICHAEL D., GUASTO, JEFFREY S., HAWARD, SIMON J., SHEN, AMY Q., HORMOZI,

- SARAH, MOROZOV, ALEXANDER, POOLE, ROBERT J., SHANKAR, V., SHAQFEH, ERIC S. G., STARK, HOLGER, STEINBERG, VICTOR, SUBRAMANIAN, GANESH & STONE, HOWARD A. 2022 Perspectives on viscoelastic flow instabilities and elastic turbulence. *Phys. Rev. Fluids* **7**, 080701.
- DEISSLER, R. G. 1986 Is navier–stokes turbulence chaotic? *Physics of Fluids* **29** (5), 1453–1457.
- DUBIEF, YVES, TERRAPON, VINCENT E. & HOF, BJÖRN 2023 Elasto-inertial turbulence. *Annual Review of Fluid Mechanics* **55** (Volume 55, 2023), 675–705.
- GARG, HIMANI, CALZAVARINI, ENRICO & BERTI, STEFANO 2021 Statistical properties of two-dimensional elastic turbulence. *Phys. Rev. E* **104**, 035103.
- GE, JIN, ROLLAND, JORAN & VASSILICOS, JOHN CHRISTOS 2023 The production of uncertainty in three-dimensional Navier–Stokes turbulence. *Journal of Fluid Mechanics* **977**, A17.
- GILLISSEN, J. J. J. 2019 Two-dimensional decaying elastoinertial turbulence. *Phys. Rev. Lett.* **123**, 144502.
- GROISMAN, A. & STEINBERG, V. 2000 Elastic turbulence in a polymer solution flow. *Nature* **405**, 53–55.
- GUPTA, ANUPAM & VINCENZI, DARIO 2019 Effect of polymer-stress diffusion in the numerical simulation of elastic turbulence. *Journal of Fluid Mechanics* **870**, 405–418.
- HAMEDUDDIN, ISMAIL, MENEVEAU, CHARLES, ZAKI, TAMER A. & GAYME, DENNICE F. 2018 Geometric decomposition of the conformation tensor in viscoelastic turbulence. *Journal of Fluid Mechanics* **842**, 395–427.
- HO, RICHARD D. J. G., CLARK, DANIEL & BERERA, ARJUN 2024 Chaotic measures as an alternative to spectral measures for analysing turbulent flow. *Atmosphere* **15** (9).
- HU, D. & LELIÈVRE, T. 2007 New entropy estimates for the Oldroyd-B model and related models. *Communications in Mathematical Sciences* **5** (4), 909 – 916.
- KHALID, MOHAMMAD, SHANKAR, V. & SUBRAMANIAN, GANESH 2021 Continuous pathway between the elasto-inertial and elastic turbulent states in viscoelastic channel flow. *Phys. Rev. Lett.* **127**, 134502.
- LANNELONGUE, LOÏC, GREALEY, JASON & INOUE, MICHAEL 2021 Green Algorithms: Quantifying the Carbon Footprint of Computation. *Advanced Science* **8** (12), 2100707.
- LELEP, MARTIN, LINKMANN, MORITZ & MOROZOV, ALEXANDER 2024 Purely elastic turbulence in pressure-driven channel flows. *Proceedings of the National Academy of Sciences* **121** (9), e2318851121.
- LEWY, THEO & KERSWELL, RICH 2024a The polymer diffusive instability in highly concentrated polymeric fluids. *Journal of Non-Newtonian Fluid Mechanics* **326**, 105212.
- LEWY, THEO & KERSWELL, RICH 2024b Revisiting 2d viscoelastic kolmogorov flow: A centre-mode-driven transition, arXiv: 2410.07402.
- MOROZOV, ALEXANDER 2022 Coherent structures in plane channel flow of dilute polymer solutions with vanishing inertia. *Phys. Rev. Lett.* **129**, 017801.
- MOROZOV, ALEXANDER N. & VAN SAARLOOS, WIM 2007 An introductory essay on subcritical instabilities and the transition to turbulence in visco-elastic parallel shear flows. *Physics Reports* **447** (3), 112–143.
- PAGE, JACOB, DUBIEF, YVES & KERSWELL, RICH R. 2020 Exact traveling wave solutions in viscoelastic channel flow. *Phys. Rev. Lett.* **125**, 154501.
- PAN, L., MOROZOV, A., WAGNER, C. & ARRATIA, P. E. 2013 Nonlinear elastic instability in channel flows at low reynolds numbers. *Phys. Rev. Lett.* **110**, 174502.
- PLAN, EMMANUEL LANCE CHRISTOPHER VI M., GUPTA, ANUPAM, VINCENZI, DARIO & GIBBON, JOHN D. 2017 Lyapunov dimension of elastic turbulence. *Journal of Fluid Mechanics* **822**, R4.
- POOLE, R.J., BUDHIRAJA, B., CAIN, A.R. & SCOTT, P.A. 2012 Emulsification using elastic turbulence. *Journal of Non-Newtonian Fluid Mechanics* **177–178**, 15–18.
- RUELLE, DAVID 1979 Microscopic fluctuations and turbulence. *Physics Letters A* **72** (2), 81–82.
- SAMANTA, DEVRANJAN, DUBIEF, YVES, HOLZNER, MARKUS, SCHÄFER, CHRISTOF, MOROZOV, ALEXANDER N., WAGNER, CHRISTIAN & HOF, BJÖRN 2013 Elasto-inertial turbulence. *Proceedings of the National Academy of Sciences* **110** (26), 10557–10562.
- SRIVASTAVA, ISHAN, NONAKA, ANDREW J., ZHANG, WEIQUN, GARCIA, ALEJANDRO L. & BELL, JOHN B. 2025 Molecular fluctuations inhibit intermittency in compressible turbulence, arXiv: 2501.06396.

- STEINBERG, VICTOR 2021 Elastic turbulence: An experimental view on inertialess random flow. *Annual Review of Fluid Mechanics* **53**, 27–58.
- SVIRSKY, ANTON & FRISHMAN, ANNA 2024 Symmetry breaking in two-dimensional turbulence induced by out-of-equilibrium fluxes, arXiv: 2410.15950.
- SVIRSKY, ANTON, HERBERT, CORENTIN & FRISHMAN, ANNA 2023 Two-dimensional turbulence with local interactions: Statistics of the condensate. *Phys. Rev. Lett.* **131**, 224003.
- THIEN, NHAN PHAN & TANNER, ROGER I. 1977 A new constitutive equation derived from network theory. *Journal of Non-Newtonian Fluid Mechanics* **2** (4), 353–365.
- TRAORE, BOUBOU, CASTELAIN, CATHY & BURGHELEA, TEODOR 2015 Efficient heat transfer in a regime of elastic turbulence. *Journal of Non-Newtonian Fluid Mechanics* **223**, 62–76.
- YERASI, SUMITHRA R., PICARDO, JASON R., GUPTA, ANUPAM & VINCENZI, DARIO 2024 Preserving large-scale features in simulations of elastic turbulence. *Journal of Fluid Mechanics* **1000**, A37.